Novel ZnO-based Ternary Oxides for Optoelectronic Applications

Mareike Trunk

Thesis submitted in partial fulfillment
of the requirements for the degree of
Philosophiae Doctor

Department of Physics
University of Oslo

August 2012

Abstract

Zinc oxide (ZnO) has been used in a wide range of products for many years, including, among others, varistors, surface acoustic wave devices and cosmetics. Besides these established applications, ZnO and its ternary alloys are now also being considered as potential materials for optoelectronic applications, such as light emitting diodes, photovoltaics, sensors, displays, etc. Unlike other materials, which could be used alternatively, ZnO has the advantage of being inexpensive, chemically stable and relatively plentiful. In spite of the long research history, fabrication of defect free ternary alloys and stable p-type ZnO is still challenging. The aim of this work was therefore to provide a better understanding of ZnO ternary alloys, so that - based on the gained knowledge - their optical properties can be further improved and, in a second step, optoelectronic applications based on these materials can soon be commercialized. The work carried out in this thesis was two-fold: the first part aimed at identifying the origin of defect related luminescence phenomena in ZnMgO, and the second part was dedicated to the exploration of a novel ZnCdO-based heterostructure photovoltaic applications.

In the case of ZnMgO, luminescence properties of deep level defects were studied by photoluminescence (PL) spectroscopy and a model was proposed to explain the changes in the deep band emission with increasing Mg content. In this model, the observed trends can be understood by considering interaction of native zinc and oxygen defects of the ZnO sublattice with Mg interstitials (Mg_i). In summary, the deep level bands at 3.0 and $2.8\,eV$, which show a blueshift with increasing Mg content, were assigned to free-to-bound type transitions between zinc interstitials (Zn_i) with the valence band edge and between the conduction band edge with zinc vacancies (V_{Zn}), respectively. A red band at $2.0\,eV$, which does not show an apparent shift of the peak energy for increasing Mg content, is associated with the oxygen vacancies (V_O). Two luminescence bands at 2.3 and $2.5\,eV$, which are redshifted for higher Mg concentrations, were assigned to transitions between zinc and oxygen interstitials and between zinc interstitials and zinc vacancies, respectively. The redshift is interpreted in terms of a competing supply of electrons from slightly deeper Mg_i donor states. The ZnMgO band gap diagram, which the model is based on, has contributed to gain valuable information about the nature of the deep defects both in ZnO and ZnMgO and is therefore of fundamental interest.

In the second part of this work, focused on ZnCdO, a stacked heterostructure was designed for

application in a photoelectrochemical cell, which is used for hydrogen production by photoelectrolysis using the semiconductor as an absorber. Optical and photoelectrochemical measurements led to the conclusion that the optical emission band for the ZnCdO heterostructures is broadened compared to a ZnO single layer. The broadened emission could be explained by combined excitonic recombination from the individual layers in the structure. The carrier dynamics in the structures were further investigated by time-resolved photoluminescence spectroscopy. A comparison of recombination parameters in ZnCdO heterostructures and in ZnO single layer films suggests a higher density of non-radiative recombination centers in the heterostructures. Furthermore, the effect of built-in fields on the carrier dynamics was assessed by investigating carrier recombination processes in a variety of different heterostructure geometries. The study does not only provide knowledge necessary to understand the origin of limiting factors in the proposed ZnCdO structure, but is also of general interest as the insight can be applied to a variety of other graded band gap type structures. Finally, photoelectrochemical testing of the ZnCdO structures confirmed the optical activity of the films, thus providing a proof of concept for the suitability of ZnCdO heterostructures as photoanodes in photoelectrochemical cells.

Acknowledgements

Like Althea Gibson once said, "No matter what accomplishments you make, somebody helped you.", this work wouldn't have been possible with the help and support of many people.

First of all, I would like to thank my main supervisor Andrej Yu. Kuznetsov for giving me the possibility to accomplish this thesis, for his support through the years and for giving me the opportunity to be part of the NanoPEC and the SolarH2 networks. I would also like to express my gratitude to my second supervisor, Augustinas Galeckas, who was always available to discuss the latest results, to answer my countless questions, to help me in the lab and to share his immense knowledge about photoluminescence. He was a great support during these years and I am very grateful for his advice, the scientific coffee breaks with him, which were always very inspiring and motivating, and the huge effort he put into proof-reading this thesis. Then I would like to say a big thank you to my third unofficial supervisor, Agnieszka Gorzkowska-Sobas, for her support in and around the photoelectrochemistry lab, for coating my samples by PLD, for the hours we spent together in the gym and last but not least for her moral support. I gratefully acknowledge my colleagues Vishnukanthan Venkatachalapathy and Tianchong Zhang, who not only did a great job with synthesizing samples for me whenever I needed them on short notice, but who were also always there to help me in the lab and to discuss results.

Our technicians Viktor Bobal and Mikael Sjödin are acknowledged for their help in the clean room and with any other lab equipment, Alexander Azarov is acknowledged for doing RBS and Tof-ERDA measurements and Øyvind Johansen from the physics workshop is acknowledged for his effort in building a new photoelectrochemical cell setup. I would also like to thank all my colleagues at MiNaLab and at SMN for the great working atmosphere. Thank you, Bahman Raeissi, Chi Kwong Tang, Hallvard Angelskår, Hans Normann, Helge Malmbekk, Lars Løvlie, Lasse Vines, Michael Böttger, Pekka Neuvonen, Per Lindberg and Vincent Quemener. And in particular, I would like to thank Ethan Long for proof-reading the whole thesis, Janicke Furberg for our coffee breaks, Klaus Magnus Håland Johansen for the help with LaTex, Knut Erik Knutsen for the good company in the office and teaching me Norwegian, Mari Alnes for her help in the ALD lab and our sunday chats at the chemistry department and Ramon Schifano for our lunches at Forskningsparken. I am really happy that I had you as colleagues!

I would also like to thank my friends in Oslo and in Germany for the fun times spent together and for distracting me from work during the evenings and weekends. So a big thank you goes to Solveig Nilsen, Christoph Sprung, Katja Kücherer, Susanne Strohmaier, Edda Blessing, the whole 'WG and friends'-gang and to my friends from my student days in Karlsruhe. You are fantastic and were a great support during the process of doing my Ph.D.

Thank you, mum and dad, for always having faith in me and being supportive wherever you can.

And last but not least, I want to thank my sister. Ina, du bist die Allerbeste!

Mareike Trunk
August 2012

Table of Contents

Chapter 1

Introduction

The focus of the thesis was the investigations of ZnCdO and ZnMgO as well as the study of graded band gap ZnCdO heterostructures for application in photoelectrochemical cells (PECs). The fundamental motivation for these studies was to explore novel materials suitable for attaining clean energy. It is commonly agreed that further development of renewable energy sources is crucial to satisfy the energy needs of our society in an environmentally friendly way. At the same time, saving energy and efficient energy utilization is equally important [1, 2]. For example, recent studies show that replacing traditional incandescent light bulbs by light emitting diodes (LEDs) saves $\sim 15\%$ of the grid energy [3]. However, until recently the efficiency of white LEDs has been a challenge. This has - among other reasons - triggered an increase in research on ZnO since the early 2000s [4]. The key properties, which make ZnO such a promising semiconductor, are its wide band gap (E_{g}) of $\sim 3.4\,\mathrm{eV}$, which corresponds to the violet/blue portion of the visible spectrum, its high exciton binding energy of $E_{\mathrm{x}} = 57\,\mathrm{meV}$, which ensures reliable performance of optoelectronic applications even at room temperature, and its abundance in the earth's crust. On top of that, the band gap of ZnO can be tuned in a wide range by alloying it with other group II metals, such as Mg, Cd, etc. Mixing ZnO with MgO, which has a band gap of $E_{\mathrm{g}} = 7.7\,\mathrm{eV}$, leads to an increase of the band gap and thus allows for optoelectronic applications in the deep UV spectral range. Furthermore, ZnMgO can be used in quantum well structures, in form of ZnMgO/ZnO/ZnMgO repetitions, assuring carrier confinement in ZnO by ZnMgO barriers [5]. Alloying ZnO with Cd, on the other hand, decreases the band gap. Depending on the Cd content, the band gap can be tuned in a wide range matching a reasonable portion of the visible solar spectrum, which makes ZnCdO a promising candidate for photovoltaic (PV)

devices. A particular example of such PV applications may be the use of ZnCdO as an electrode in PEC devices for solar hydrogen production by photoelectrolysis of H_2O [6]. In order to drive the water splitting process, the semiconductor has to fulfill several requirements, including the width of the band gap, the position of the band edges against the H_2O redox potentials and the resistance to (photo)corrosion [7]. In PECs, a metal back contact is used to extract electrons from the active semiconductor region, while most other optoelectronic devices, for instance solar cells and LEDs, need both n- and p-type type materials. Zn(Cd)O exhibits native n-type conductivity, while stable and low-resistive p-type Zn(Cd)O has not yet been established [8, 9]. In this sense, the use of Zn(Cd)O in PECs is very appropriate, since only a metal back contact is needed in order to fully exploit the excellent light absorbing properties of ZnCdO. The efficiency in the PECs may be further increased by enhancing the light absorption, for instance by stacking ZnCdO films with various band gaps on top of each other. Considering that the fabrication of high-quality ZnCdO and ZnMgO films has reached a mature stage, examination of their optical properties is timely and well motivated in order to use these materials for energy generation and saving technologies.

The present thesis is organized in four main chapters. First, a short literature survey on properties of pure ZnO and its ZnCdO and ZnMgO alloys is provided in Chapter 2. Special emphasis is put on excitonic and deep level transitions in ZnO, which is used as a base line in the thesis. Secondly, Chapter 3 explains the principle of PECs and motivates for the use of Zn(Cd)O multilayers as active elements in these devices. Following that, an overview of the experimental techniques employed for optical, structural and photoelectrochemical characterization of the samples is given in Chapter 4. Finally, Chapter 5 highlights the findings, which were obtained in this work and published in the articles attached to this thesis, and concluding remarks and suggestions for further work are presented in Chapter 6.

Chapter 2

ZnO and its alloys with CdO and MgO

This chapter introduces the key material properties of ZnO and its alloys ZnCdO and ZnMgO. The lattice structure and synthesis of ZnO is subject of the first section. Thereafter, the electronic band structure and the effect of Cd and Mg alloying are discussed. Finally, the optical properties including a summary of the deep level emission and the carrier lifetimes in Zn(Cd,Mg)O are presented.

2.1 Structural properties and synthesis

ZnO belongs to the group of II-VI semiconductors and crystallizes in the hexagonal wurtzite (wz) structure, which is illustrated in Fig. 2.1 (a). The hexagonal lattice parameters are $a = b = 0.325\,\text{nm}$ and $c = 0.520\,\text{nm}$ [10]. Crystallization of ZnO in the wz structure instead of rocksalt (rs, see Fig. 2.1 (b)) and zincblende (zb, see Fig. 2.1 (c)) is due to the strong bond polarity between the oxygen and the zinc atoms in the crystal. The covalent ZnO binding consists of four equal sp^3 orbitals with the binding sp^3 states forming the valence band and the anti-bonding states form the conduction band. For lower bond polarity, which is the case in many III-V semiconductors, crystallization in zb structure is usually favored [10]. For ZnO, the zb structure is only obtained under certain growth conditions, for instance, growth on a zb substrate [11]. The big difference in the electronegativity of oxygen and zinc is also the reason that the ZnO binding is on the border between being covalent (typical for semiconductors) and ionic (typical for insulators). The corresponding ionic radii of the cation (Zn^{+2}) and the anion (O^{-2}) are $0.074\,\text{nm}$ and $0.140\,\text{nm}$, respectively [12]. The rs structure, which is common for ionically bound crystals,
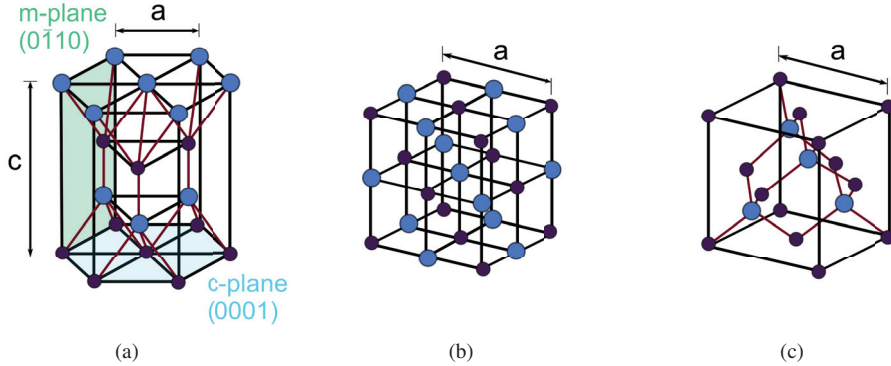
Figure 2.1: *ZnO crystal structures: The hexagonal wurtzite (a), the cubic rock salt (b) and zinc blende structure (c). The smaller (black) and bigger (blue) circles represent the cations and anions, respectively.*

can be found for ZnO under certain growth conditions, for instance, under alloying with CdO or MgO.

Various substrates and epitaxial techniques have been explored to optimize the growth of ZnO. While hydrothermal bulk growth, vapor phase transport, chemical transport techniques and flux growth techniques are standard techniques for fabrication of bulk ZnO, metal organic vapor phase epitaxy (MOVPE), molecular beam epitaxy (MBE), pulsed laser deposition (PLD) and atomic layer deposition (ALD) are used to develop advanced structures and for research purposes [13]. In this work, MOVPE was the growth method of choice, since it offers large versatility, both in terms of precursor choice (material) and growth control (advanced heterostructures). The precursors used for growth of ZnO were diethylzinc (DEZn) and *tert*-butanol (t-BuOH). In addition, dimethyl cadmium (DMCd) and bis-cyclopentadienyl-magnesium (Cp$_2$Mg) were applied to achieve Cd and Mg doping, respectively. Further details about MOVPE growth technique and the specific commercial reactor (TITAN/EMF), which was employed for growth, can be found in [14].

2.2 Electronic properties

The electronic band structure of wz ZnO is characterized by a direct band gap at the Γ-point, as can be seen in a local density approximation + Coulomb interaction (LDA + U) calculation
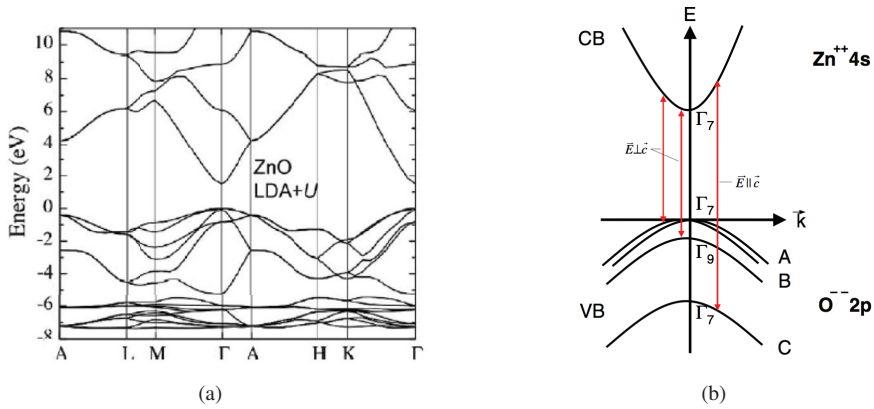
Figure 2.2: *Electronic structure of ZnO: (a) calculated band structure taken from [17] showing a direct bandgap at the Γ-point, (b) illustration of the valence band splitting at the Γ-point taken from [18], which is due to the hexagonal crystal field and spin-orbit coupling.*

depicted in Fig. 2.2 (a), with the conduction band (CB) mainly originating from empty antibonding sp^3 orbitals or 4s states of Zn^{+2} and with the valence band (VB) mainly being formed by bonding sp^3 hybrid states or 2p states of O^{-2}. Due to the hexagonal crystal field in the wz ZnO and due to spin-orbit coupling, the valence band is split into three twofold-degenerate states, as illustrated in Fig. 2.2 (b) [10, 15]. Experimentally measured values of the ZnO band gap range between $3.44\,\text{eV}$ at $10\,\text{K}$ and $\sim 3.3\,\text{eV}$ at room temperature [16]. The disagreement between experimental and theoretical data ($1.51\,\text{eV}$ in Fig. 2.2 (a)) is common for LDA and is mainly due to discontinuities in the derivative of the exchange-correlation energy [15].

Band gap engineering

The replacement of Zn by another cation readily changes the band structure and the band gap accordingly. In this work, we have concentrated on alloying ZnO by adding Mg and Cd, which allows for variation of the band gap from high in the ultra-violet (UV) down to the green-yellow visible part in the spectrum, respectively. The band gap of $Zn_{1-x}Mg_xO$ can be tuned in the range between $3.4\,\text{eV}$ and $7.8\,\text{eV}$ (MgO) [19]. Theoretical studies reveal that the increase of the band gap is mostly due to Mg 3s-like states, which shift the CB states to higher values. From a crystallographic point of view, however, the mixing of ZnO and MgO is not trivial, since MgO crystallizes in rs structure (see Fig. 2.1 (b)). At equilibrium, the solubility of Mg ions in a ZnO lattice was estimated to be as low as $x = 0.04$ [20]. Yet, $Zn_{1-x}Mg_xO$ growth far
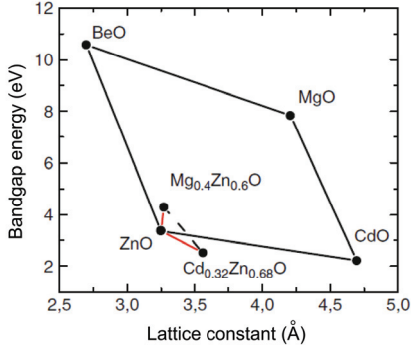
Figure 2.3: *Key band gap and lattice parameters for ZnO and related oxides and alloys, taken from [10].*

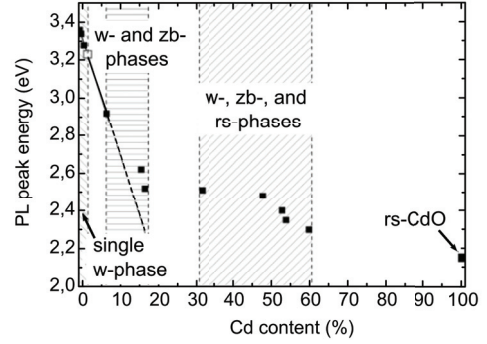**Figure 2.4:** *Phase separation in ZnCd$_x$O taken from [24]. For $0.07 < x < 0.17$ phase separation between wz- and zb-phases, for $x > 0.17$ wz-, zb- and rs-phases coexist.*

from equilibrium makes higher Mg concentrations up to $x \sim 0.4$ possible, with the wz crystal structure still being preserved. At room temperature, the band gap of wz Zn$_{1-x}$Mg$_x$O follows $E_g(x) = (3.32 + 2.00x)\,\text{eV}$ [21]. For $x > 0.6$, the alloy crystallizes in rs structure with the band gap changing according to $E_g(x) = (3.02 + 4.03x)\,\text{eV}$ [21]. Between $x = 0.4$ and 0.6, the band gap is not well defined since phase separation occurs [19].

As pointed out earlier, Zn$_{1-x}$Cd$_x$O is characterized by a band gap in the visible range due to the direct band gap of CdO being $2.3\,\text{eV}$ [22]. The decrease of the band gap is mostly due to an intermixing of Zn 3d-like and Cd 4d-like states, which effectively lowers the conduction band minimum. However, as CdO has a rs structure (see Fig. 2.1 (b)), the synthesis of ZnCdO is complicated and the solid solubility of Cd is limited to $x = 0.04$ for equilibrium growth conditions [10]. Yet, higher Cd concentrations can be obtained by growth of Zn$_{1-x}$Cd$_x$O far from equilibrium and thus concentrations up to $x = 0.69$ have been achieved [23]. At higher Cd concentrations, due to the different crystallographic structures, phase separation occurs, where both wz and zb phases $(0.07 < x < 0.17)$ and wz, zb and rs phases $(0.17 < x < 0.60)$ coexist (see Fig. 2.4) [24].

2.3   Optical properties

The luminescent transitions, which are commonly observed in ZnO, are illustrated in Fig. 2.5. As shown in panel (a), the recombination of a free electron at the bottom of the conduction band
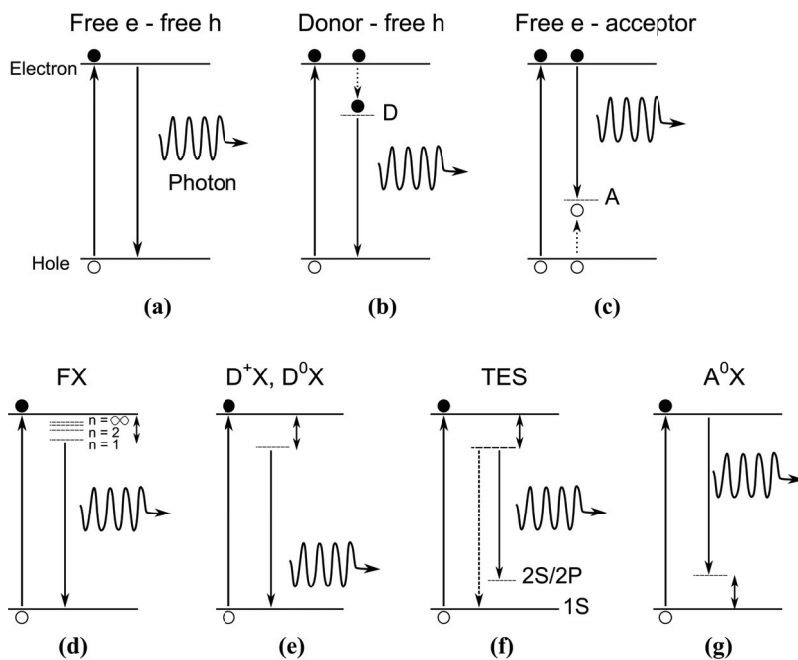
Figure 2.5: *Near band edge emission in ZnO: The photon energy $E_{h\nu}$ equals the band gap energy for free carrier recombination (a) and is reduced accordingly if donor or acceptor states (b, c) or excitons (d)-(g) are involved. Besides free exciton (FX) transitions, donor bound (D^0X, D^+X) and acceptor bound (A^0X) excitons as well as two electron satellites (TES) are observed.*

and a free hole at the top of the valence band, gives rise to photons with an energy corresponding to the band gap. The photon energy is accordingly reduced, if the transition takes place via donor or acceptor states (see Fig. 2.5 (b)/(c)). A reduction of the photon energy is also observed in the likely case of exciton formation in the semiconductor. The corresponding excitonic transitions are depicted in Fig. 2.5 (d)-(g). As the exciton quasiparticle is a hydrogen-like state of an electron and a hole attracted to each other by Coulombic force, the binding energy can be estimated by a hydrogen atom, where the electron orbits the hole. If the exciton is not spatially localized, i.e. highly localized in k-space, one speaks of a *free exciton* (FX), as depicted in Fig. 2.5 (d). The photons, which are emitted if a FX recombines, correspond therefore to the band gap value reduced by the exciton energy E_x:

$$h\nu = E_\mathrm{FX} = E_\mathrm{g} - E_\mathrm{x} \qquad \text{with} \qquad E_\mathrm{x} = R_y^* \frac{1}{n^2} = 13.6\,\mathrm{eV}\,\frac{\mu}{n^2 \epsilon_0^2} \qquad (2.1)$$

where μ is the reduced electron-hole mass. In ZnO, excitons are present even at room temperature, since E_x is as large as $57\,\mathrm{meV}$, which is comparable to the thermal activation energy at $T \gg 600\,\mathrm{K}$. The exciton can be bound to a dopant or an impurity atom, in which case one refers to the exciton and the corresponding optical signature as a *bound exciton* (BX), illustrated in Fig. 2.5 (e)-(g). The photon energy of bound excitons is reduced by the dopant/impurity-specific exciton localization (or binding) energy E_B compared to the energy of FX recombination:

$$h\nu = E_\mathrm{BX} = E_\mathrm{g} - E_\mathrm{x} - E_\mathrm{B} \qquad (2.2)$$

One distinguishes between excitons bound to ionized acceptors (A^-X), to neutral acceptors (A^0X), to ionized donors (D^+X) and to neutral donors (D^0X). Ionized acceptors, however, are not found in ZnO, since other excitons are energetically favorable. The D^+X is comparable to a H_2^+ molecule, therefore its binding energy can be approximated by

$$E_{D^+X} \leq \frac{H_2^+}{H} E_\mathrm{x} \approx 0.19 E_\mathrm{x} \qquad (2.3)$$

In ZnO, excitons bound to D^+X show up at energies $\sim 10-20\,\mathrm{meV}$ below the free exciton line. Excitons bound to a neutral donor, on the other hand, resemble the H^2 molecule with

$$E_{D^0X} \leq \frac{H_2}{H} E_\mathrm{x} \approx 0.33 E_\mathrm{x} \qquad (2.4)$$

Excitons bound to neutral donors are therefore found at lower energies than excitons bound to ionized donors. At even lower energies, neutral acceptor-related exciton peaks are found. During recombination of neutral donor bound excitons, it is possible, that the donor is left in an excited state, the 2s/2p state, instead of the 1s ground state. The corresponding transition is known as a two-electron satellite (TES) line, and the energy difference between the D^0X and the TES line corresponds to the energy difference between the 1s ground and the 2s/2p state:

$$E_{\text{TES}} = E_{D^0X} - \Delta E = E_{D^0X} - (E_{D(1s)} - E_{D(2s)}) \tag{2.5}$$

The above described emission lines lie close to the band edge and are commonly referred to as near band edge (NBE) emission.

Defect states and related emission

In addition to near band edge emission, a characteristic deep level (DL) emission band is observed in ZnO, the origin of which is recombination via defect states located deep in the forbidden band gap. If the DL is acceptor (donor) like, a free electron (hole) recombines with the hole (electron) bound to the deep state. Since the bound carrier is localized in the crystal, the recombination process will lead to lattice relaxation. Therefore, a part of the energy is released as phonons, and the DL peaks become broad. While the assignment of the NBE emission to specific dopants or defects in the crystal is rather straight forward, the interpretation of DL emission in ZnO has been debated. In particular, the interpretation of the transitions with $E \sim 2.4\,\text{eV}$ in ZnO, the so-called green luminescence (GL), has been the subject of many articles and for a long time the V_O related donor was erroneously believed to cause this band [25]. The GL has not yet been assigned to a specific defect, but it could be verified that a transition from the V_O donor level to the VBM is not the origin of this band [26]. Yet, first-principle calculations show that the V_O causes a deep donor state, which lies around 1.0 to $1.3\,\text{eV}$ below the CBM [27, 28]. The formation of oxygen interstitials (O_i), on the other hand, yields acceptors enabling a recombination of conduction band electrons with holes trapped at these defects. Depending on the transition level, the calculated O_i energy states are around $0.72\,\text{eV}$ ($\epsilon(0/-)$) and around $1.59\,\text{eV}$ ($\epsilon(-/2-)$) above the VBM, respectively [27]. The violet-blue emission in ZnO with $\lambda \sim 410\,\text{nm}$ has been assigned to a transition from the shallow Zn_i donor state to the VB [29], based on theoretically predicted positions of the Zn_i level [28, 30]. The presence of V_{Zn}, on the other side, leads to the formation of acceptor states around $0.4\,\text{eV}$ above the VB [27, 28, 31]. Therefore, it has been suggested that the blue PL band peaking at $\sim 470\,\text{nm}$ is due to a CB to V_{Zn} transition

[29]. Further bands which are commonly observed in ZnO are at $\sim 1.9\,\text{eV}$ (red), $\sim 2.05\,\text{eV}$ (orange) and $\sim 2.15\,\text{eV}$ (yellow) [32]. The red-orange emission ($\sim 2.0\,\text{eV}$) was claimed to be related to V_O by Vlasenko and Watkins [26], while the yellow band was proposed to be due to a donor acceptor pair transition. Reshchikov et al. [32] tentatively assigned the deep acceptor to V_{Zn} complexes.

Carrier lifetime in ZnO

The carrier lifetime is a basic parameter, which is used to assess the quality of semiconductor materials and devices, respectively. It is defined as the time between generation and recombination of a carrier and can, for instance, be determined by means of time-resolved photoluminescence [33]. Further details about the time-resolved photoluminescence spectroscopy and carrier recombination processes in semiconductors are discussed in section 4.1. Lifetime values vary depending on the carrier concentration in the semiconductor, the temperature, the surface, the interface, etc., but as a general rule, the better the crystal quality is, the longer the lifetime becomes. The carrier lifetime in ZnO is typically in the range between a few hundred picoseconds to a few nanoseconds [34, 35, 36]. Chichibu et al.[37] report about the improvement of ZnO epilayer films by the elimination of point defects by variation of different growth parameters including substrate choice, growth temperature, annealing time and pressure. The effective carrier lifetime τ_{PL} at the NBE peak energy in the improved ZnO epilayer film, which was grown by MBE using a ZnO buffer layer, is characterized by $\tau_{PL} = 1.34\,\text{ns}$ at $293\,\text{K}$ compared to $\tau_{PL} = 0.97\,\text{ns}$ measured in bulk ZnO and $\tau_{PL} = 0.11\,\text{ns}$ in ZnO epilayers grown on a ScAlMgO$_4$ substrate. The corresponding non-radiative and radiative components at room temperature were $\tau_{nr} = 1.31\,\text{ns}$ and $\tau_r = 20.6\,\text{ns}$. These values are in good agreement with other carrier lifetimes measured in ZnO. For comparison, in ZnMgO epilayers grown using the same ZnO buffer layer, the carrier lifetime at the NBE PL peak at room temperature is as small as $0.06\,\text{ns}$ with the radiative and the non-radiative component being $\tau_r = 75.4\,\text{ns}$ and $\tau_{nr} = 0.03\,\text{ns}$, respectively. The decrease of τ_{nr} by about two orders of magnitude indicates a high density of non-radiative recombination centers [38]. Similarly, the carrier lifetime in wz $Zn_{1-x}Cd_xO$ epilayers is $\sim 0.05\,\text{ns}$ at the peak energy for $x = 0.09$ and dropped to $\tau_{PL} \sim 0.02\,ns$ for $x = 0.16$ [39].

Chapter 3

Photoelectrochemical water splitting

In the search for environmentally friendly energy sources, the production of hydrogen by solar energy conversion is a promising alternative, since hydrogen can be inexpensively converted back to electricity or can be used as a fuel directly. Compared to other chemical fuels, as for instance methane, gasoline, etc., solar hydrogen production appears to be a more attractive way, since only water and light as plentiful energy sources and hydrogen and oxygen as clean products are involved in the process. The redox reaction, that describes generation of hydrogen by photoelectrochemical splitting of water into H_2 and O_2, is endothermic and requires an energy of $\Delta G = 237 \, kJ/mol$. The overall reaction can be written as follows [40]:

$$2H_2O \longrightarrow O_2 + 2H_2 \tag{3.1}$$

3.1 The photoelectrochemical cell

Photoelectrolysis can be accomplished in photoelectrochemical cells (PECs), which are typically composed of a semiconductor and a metal electrode connected ohmically and immersed in a water-based electrolyte. As illustrated in Fig. 3.1, the sunlight is absorbed in a semiconductor electrode and electron-hole pairs are generated. The electrons and holes are thereafter separated across a depletion region, which is due to the band bending at the semiconductor-electrolyte interface (see Fig. 3.2). When a semiconductor is brought into contact with a metal or a liquid, a movement of charge will set in to achieve equilibrium of the two materials. The direction of charge flow is determined by the relative position of the Fermi levels or, in an electrolyte, by the
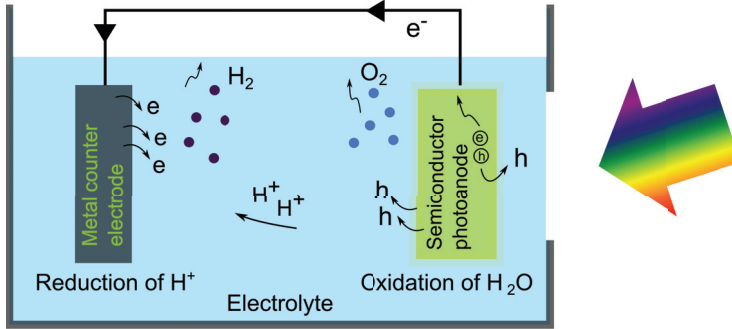
Figure 3.1: *Principle of a photoelectrochemical cell: A semiconductor and a metal electrode are connected ohmically and immersed in an electrolyte. Upon illumination, electron-hole pairs are generated in the semiconductor. The carriers, separated across the depletion region at the semiconductor-electrolyte interface, are transferred to the water solution, where they split the H_2O molecules generating hydrogen.*

position of the redox potential. As the carrier density is small in a semiconductor, a space charge region forms below the surface. For an n-type semiconductor a positive space charge is generally associated with an upward band bending. Due to the upward band banding, the holes are directly injected into the electrolyte, whereas the electrons are driven towards the metal and further into the electrolyte. Therefore, the n-type semiconductor works as an anode, and the released holes oxidize the water molecules:

$$2H_2O\,(l) + 4h^+ \longrightarrow 4H^+ + O_2\,(g) \tag{3.2}$$
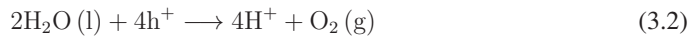
At the cathodic metal-electrolyte interface, electrons reduce H^+ resulting in hydrogen generation:

$$2H^+ + 2e^- \longrightarrow H_2\,(g) \tag{3.3}$$

Required semiconductor properties

The properties of the semiconductor electrode have to fulfill several requirements in order to drive the water splitting reaction described in Eq. 3.1. The band gap required to decompose H_2O electrochemically is determined by the standard free enthalpy per mole for this reaction

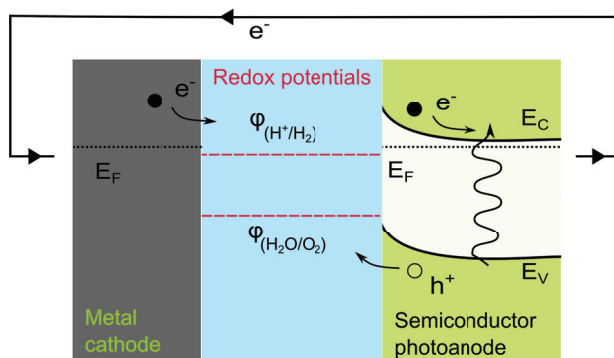$$E_g = \frac{\Delta G^0_{(H_2O)}}{2N_A} \tag{3.4}$$

Figure 3.2: *Energy diagram for a PEC illustrating the band bending at the semiconductor-electrolyte interface for an n-type photoanode. The upward band banding, induced by positive space charges, drives the holes into the electrolyte and the electrons towards the metal. ϕ_{H_2/H^+} and ϕ_{H_2O/O_2} denote the redox potentials of the electrolyte.*

where N_A is Avogadro's number. The required energy of the absorbed photons and of the band gap, respectively, amounts therefore to $1.23\,\mathrm{eV}$ [7]. In addition, overpotentials, which are due to kinetic inhibition of a reaction step (empirically in the range of $0.2\,\mathrm{eV}$), have to be taken into account. Thus, in practice, the band gap has to be larger than $1.5\,\mathrm{eV}$. Furthermore, it is desirable that the semiconductor band gap is tunable above $1.5\,\mathrm{eV}$ in order to achieve efficient absorption in the visible part of the solar spectrum. Aside from the width of the band gap, the position of the conduction (E_C) and the valence (E_V) band edges with respect to the redox potentials of the electrolyte is important. The conduction band edge has to lie above the oxidation potential, which is at $\phi_{H_2O/O_2} = (1.23 - 0.060 \cdot \mathrm{pH})\,\mathrm{V}$ with reference to the SHE (standard hydrogen electrode) level, and the valence band edge has to lie below the reduction potential, which is at $\phi_{H_2/H^+} = (-0.060 \cdot \mathrm{pH})\,\mathrm{V}$ vs. SHE (see Fig. 3.2). Furthermore, the electrode material has to be corrosion resistant in the respective electrolyte to guarantee long time durability of the cells.

3.2 Oxides as PEC electrodes

Several types of materials have been suggested as photoelectrodes. The most frequently studied semiconductor for the photoanode is TiO_2, which was also used in the pioneering works in the early 1970s [41]. The interest in oxides is in part due to their generally good anti-corrosive
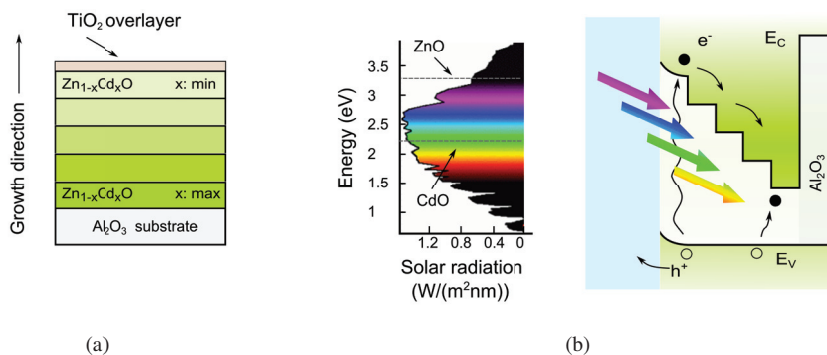
Figure 3.3: *Advanced photoanode combining a ZnCdO mulitlayered absorber and a TiO$_2$ anticorrosion overlayer (a). The stacked ZnCdO anode structure increases the efficiency, since photons from a wide range of the visible solar spectrum can be absorbed (b).*

properties and comparatively easy synthesis [42]. However, none of the existing semiconductors satisfy both chemical stability and band edge requirements. TiO$_2$, for instance, which is corrosion resistant, does not absorb sun light efficiently enough due to its wide band gap of $\sim 3.2\,\text{eV}$ (anatase phase). In contrast, the most promising electrodes in terms of the band structure are not stable in aqueous solutions [7]. Hence, a single semiconductor is not sufficient for efficient and reliable hydrogen production and trade-offs have to be made. One approach is to cover a light absorbing structure with a chemically stable protecting layer thin enough to allow for carrier tunneling. The electrode design illustrated in Fig. 3.3 (a), which was studied in the course of this work, combines the required properties.

For efficient performance of the photoelectrochemical cell, it is crucial that the band gap of the absorbing semiconductor electrode is tunable in the range between 1.5 and $3.0\,\text{eV}$. This can be achieved by employing Zn$_{1-x}$Cd$_x$O alloys, the band gap of which matches a significant part of the solar spectrum, which is of interest for photoelectrochemical applications. The absorption efficiency of the cell can be further increased by stacking several layers of ZnCdO with various Cd content as illustrated in Fig. 3.3 (b). This design makes it possible to absorb photons with different energies without substantial losses due to generation of heat. With pure ZnO as a top layer, it is furthermore assured that the conduction band edge is located energetically higher than the reduction level [43]. However, ZnO dissolves in most electrolytes making an anticorrosion layer indispensable [44]. Among other oxides, TiO$_2$ is known to be chemically stable, making it a potential candidate for a thin photoanode overlayer preventing corrosion of the underlying

electrode [45]. Aside from efficient absorption, a built-in field, which arises from the staggered band gap, may allow for more efficient charge separation [46]. However, at the same time, the advanced cell structures, which are needed to create intrinsic fields, bear the potential of deteriorated material properties. Indeed, theoretical investigations show that built-in fields in graded solar cells can be either be beneficial or deleterious [47] making a thorough study of the structures by experimental means indispensable.

Chapter 4

Methodology

This chapter gives an overview of the characterization methods used in the course of this thesis. In the first section, continuous wave (cw) and time-resolved photoluminescence techniques, which were extensively employed to study the optical properties of the samples including carrier lifetimes, are described in detail. Thereafter, in section 4.2, transmittance and diffuse reflectance measurements are presented, which were, among other things, used in order to study the absorption characteristics and carrier generation profiles of the ZnCdO structures. The photoelectrochemical characterization of the samples by voltammetry is subject to section 4.3. Finally, section 4.4, 4.5 and 4.6 describe the background for techniques used for chemical and structural analysis including rutherford backscattering spectroscopy (RBS), time-of-flight elastic recoil detection analysis (Tof-ERDA), x-ray diffraction analysis (XRD) and secondary electron microscopy (SEM).

4.1 Photoluminescence spectroscopy

Photoluminescence (PL) is a nondestructive characterization technique, where optical excitation induces luminescence, i.e. the spontaneous emission of light, which is thereafter collected by an objective and spectrally analyzed. The optical excitation is usually provided by laser light. PL spectra give information about the electronic structure of the probed material, including information about the band gap, impurity levels and alloy composition. In addition, if pulsed laser light is used for excitation, information about the carrier lifetimes and recombination mechanisms can

be obtained. In this case, a photon counting unit is needed for data acquisition in addition to the spectrometer, and one refers to the method as time-resolved photoluminescence (TRPL).

4.1.1   Instrumentation

A typical experimental setup used for PL measurements is schematically shown in Fig. 4.1. By a combination of lenses and mirrors, the laser light is focused onto the samples, which are placed in a cryostat. In this work, a closed-cycle He-refrigerator was used allowing for temperature dependent studies between $10\,\mathrm{K}$ and $300\,\mathrm{K}$. For steady-state PL measurements, a cw HeCd laser with an output power of $P = 10\,\mathrm{mW}$ operating at $\lambda = 325\,\mathrm{nm}$ was employed, and TRPL was studied by using the $372\,\mathrm{nm}$ excitation of a picosecond laser (LDH375 PicoQuant) with a FWHM of the pulses of $50\,\mathrm{ps}$ and an average power of $2\,\mathrm{mW}$ at $40\,\mathrm{MHz}$. The light emitted from the sample is collected by a microscope and directed to a fiber optic spectrometer for steady state PL (USB4000 with $2\,\mathrm{nm}$ or HR4000 with $0.2\,\mathrm{nm}$ resolution, both Ocean Optics Inc.) and to an imaging spectrograph for TRPL (iHR320, Horiba Jobin-Yvon). The latter one is combined with a TCSPC/MCS photon-counting system for time-correlated single photon counting analysis (timeHARP/ nanoHARP, PicoQuant GmbH).

4.1.2   Theoretical background

Generally, two physical processes take place during a PL measurement - firstly, the generation of carriers due to absorption of laser light in the material, and secondly, the recombination of the same carriers resulting in characteristic luminescence spectra. Naturally, both the generation rate G and the recombination rate R depend on the properties of the semiconducting material. In addition, in most materials, the absorption coefficient α, and thus also G, is dependent from the laser wavelength used for excitation. The same holds for the penetration depth d_p of the laser, given by the reciprocal of the absorption coefficient α, so that different depths in the sample can be probed depending on the excitation wavelength. In ZnO material, the lasers used in our setup have typical penetration depths of around $100\,\mathrm{nm}$ (HeCd laser) and $> 300\,\mathrm{nm}$ (Diode laser). Aside from the wavelength dependent absorption depths, the laser energy must exceed the band gap of the semiconductor sample in order to generate electrons and holes in the first place. Once electron-hole pairs have been generated, recombination processes take place to restore the carrier concentration to its thermal equilibrium value with a characteristic time constant referred to as
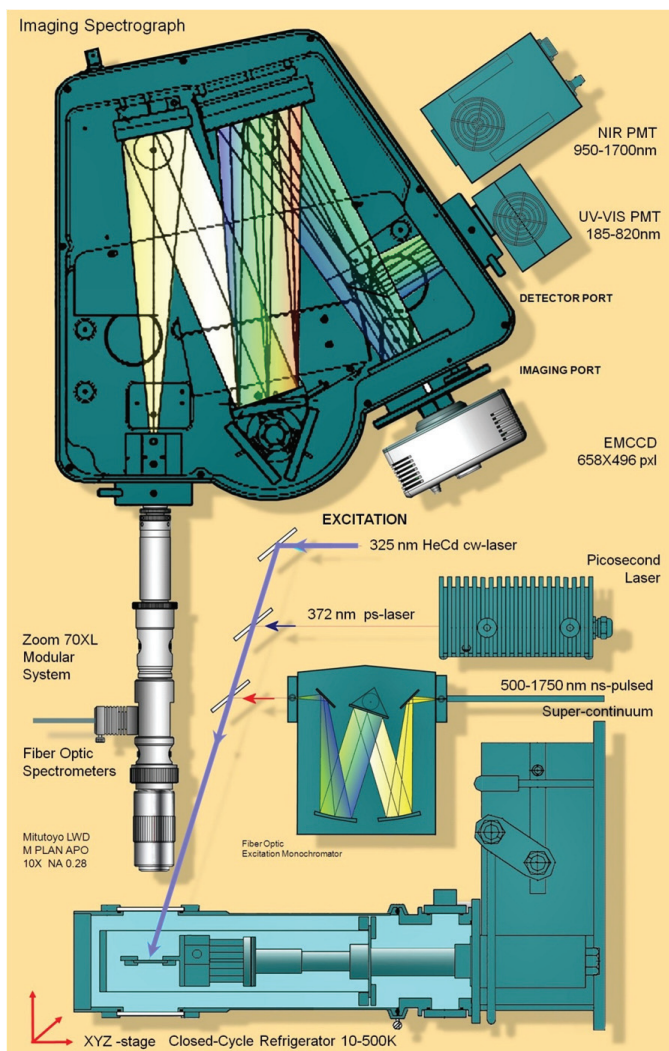
Figure 4.1: *Illustration of the PL principle, where laser light induces luminescence. The emitted light, which gives information about the electronic structure of the probed material, is collected by an objective and spectrally analyzed either by a fiber optic spectrometer or an imaging spectrograph. For carrier lifetime studies by TRPL, pulsed laser light is used for excitation and a photon counting unit is used for data acquisition in combination with the spectrograph.*

Figure 4.2: *Schematics of the three recombination mechanisms: (a) direct band-to-band radiative recombination, (b) indirect phonon-assisted recombination and (c) Auger recombination.*

the carrier lifetime τ. In an n-type semiconductor, the excess minority carrier lifetime (here holes) can be expressed by [33]

$$\Delta p(t) = \Delta p(0) \exp\left(-\frac{t}{\tau_{\mathrm{p}}}\right) \tag{4.1}$$
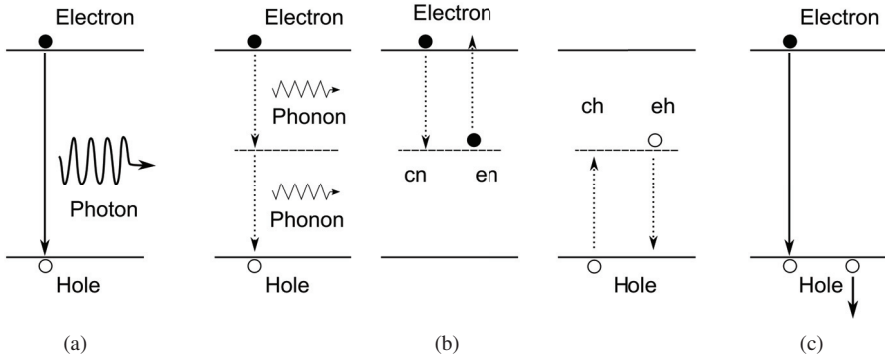
where $\Delta p(t)$ is the excess carrier (hole) concentration. Equation 4.1 shows that $\Delta p(t)$ decays with a time constant τ_{p}. Thus, the lifetime can be determined by the time in which the excess carrier concentration has reached $1/e$ of its initial value [33]. Three different kinds of transitions are usually used to describe the recombination mechanisms of the electrons and holes, namely direct band-to-band recombination, phonon-assisted Shockley-Read-Hall (SRH) recombination and Auger recombination. Depending on the mechanism, the surplus energy is released in the form of photons, phonons or is given to a third particle, as illustrated in Fig. 4.2. Each of the processes features a lifetime characteristic to the process. The effective lifetime in the material can be expressed by the sum of the inverses [33]

$$\frac{1}{\tau_{eff}} = \frac{1}{\tau_{direct}} + \frac{1}{\tau_{SRH}} + \frac{1}{\tau_{Auger}} \tag{4.2}$$

Direct or band-to-band radiative recombination

The energy, which is emitted by radiative band-to-band recombination, as schematically illustrated in Fig. 4.2 (a), approximately equals the energy difference between the involved bands. As pointed out in section 2.3, due to the presence of excitons in the crystal, the photon energy is reduced by an amount equal to the material-specific exciton energy E_x. If the exciton is bound to an impurity level, the photon energy is further reduced by the exciton binding energy E_B of the respective impurity. In nondegenerate semiconductors, radiative recombination processes are proportional to the product of electron and hole densities np, since both an electron and a hole must be present for annihilation. In an n-type semiconductor, the recombination rate R can be obtained by [33]

$$R = B_r np \tag{4.3}$$

with $n = n_0 + \Delta n$, $p = p_0 + \Delta p$ and B_r the constant of proportionality (rate of radiative capture probability). In thermal equilibrium, the rate of thermal generation G_0 equals the band-to-band radiative recombination rate R_0:

$$G_0 = R_0 = B_r n_0 p_0 = B_r n_i^2 \tag{4.4}$$

In the limit of low injection, the majority carrier concentration does not change significantly, so that n equals n_0. The net recombination rate U_r can therewith be approximated by

$$U_r = R - G_0 = B_r n_0 p - B_r n_0 p_0 = B_r n_0 \Delta p \tag{4.5}$$

and hence the radiative lifetime simplifies to

$$\tau_{r(\text{direct,low})} = \frac{\Delta p}{U_r} = \frac{1}{B_r n_0} \tag{4.6}$$

Phonon-assisted Shockley-Read-Hall recombination

If a deep level state, which can for instance be due to the presence of impurity atoms or structural defects, is involved in the transition process and serves as a intermediate state, one refers to it as trap-assisted or Shockley Read Hall (SRH) recombination, which is illustrated in Fig. 4.2 (b). SRH recombination involves two steps: In a first step, the electron (hole) is captured by the trap state. In a second step, annihilation between the electron (hole) in the trap state and

a hole in the VB (electron in the CB) takes place and energy is released via phonon emission. Trap assisted recombination is proportional to the dominant carrier density and is favored under low injection rates, as the traps, which are energetically favorable, will be filled before other states will be filled. The steady-state recombination rate for this process can be described by the rates of the four basic processes involved. These four processes are depicted in Fig. 4.2 (b) and comprise (from left to right) electron capture (cn), electron emission (en), hole capture (ch) and hole emission (eh). The net rate of electron and hole capture, respectively, under steady-state can be expressed by [48]

$$U_n = U_{cn} - U_{en} = c_n N_t (n(1 - f_t) - n_1 f_t) \tag{4.7}$$

$$U_p = U_{cp} - U_{ep} = c_p N_t (p f_t - p_1 (1 - f_t)) \tag{4.8}$$

where N_t denotes the recombination centre concentration, c_n (c_p) the electron (hole) capture coefficient and n_1 (p_1) the electron (hole) density, when the trap state is at the Fermi level. The electron capture coefficient c_n is given by $c_n = \nu_{th} \sigma_n$, where $\nu_{th} \equiv \sqrt{3kT/m}$ is the thermal velocity of the carriers and σ_h the capture cross-section of the electrons. Similarly, the hole capture coefficient can be expressed by $c_p = \nu_{th} \sigma_p$. The probability of occupation of a centre by an electron f_t given by

$$f_t = \frac{1}{1 + \exp\left((E_t - E_f)/kT\right)} \tag{4.9}$$

where E_t is the energy level of the trap. In steady-state, the net recombination rate U_{SRH} can be expressed by [33]:

$$U_{SRH} = U_n = U_p = \frac{\sigma_p \sigma_n N_t \nu_{th} (pn - n_i^2)}{\sigma_n(n + n_i \exp\left(\frac{E_t - E_i}{kT}\right)) + \sigma_p(p + n_i \exp\left(\frac{E_i - E_t}{kT}\right))} \tag{4.10}$$

where E_i is the intrinsic energy level. If the capture cross-section for electrons equals the capture cross-section for holes, $\sigma_n = \sigma_p = \sigma$, the net recombination rate for SRH reduces to

$$U_{SRH} = \frac{pn - n_i^2}{p + n + 2n_i cosh(\frac{E_i - E_t}{kT})} N_t \nu_{th} \sigma \tag{4.11}$$

Generally, trap states can either act as radiative or non-radiative centers. Shallow acceptors or donors are more likely to participate in radiative recombination, while deep states tend to cause non-radiative SRH recombination.

Auger recombination

A third form of recombination is the so called Auger recombination. In this process, the energy, which is released during recombination, is given to a third particle (electron or hole) in form of kinetic energy. Since three particles are involved, Auger recombination is only relevant under high excitation intensities. The net recombination rate for the Auger process can be calculated by [48]

$$U_{Auger} = C_\mathrm{n}(n^2 p - n_0^2 p_0) + C_\mathrm{p}(p^2 n - p_0^2 n_0) \tag{4.12}$$

where C_n and C_n are the probability coefficients for electron and hole emission, respectively.

4.1.3   Data analysis

Steady state photoluminescence

PL spectroscopy offers several means to discriminate between the various intrinsic and extrinsic properties presented above and in section 2.3. *Temperature dependent PL* allows for determination of thermal activation parameters, of the band gap narrowing parameters and of the internal quantum efficiency $\eta_\mathrm{int}^\mathrm{eq}$. The activation energy E_a of a certain PL peak can be determined by monitoring the intensity at the peak specific wavelength against the temperature and fitting the data by an Arrhenius function

$$I(T) = \frac{I_0}{1 + A exp(-E_\mathrm{a}/kT)} \tag{4.13}$$

where I_0 is the PL intensity at low temperature and A is a variable. At the same time, the internal quantum efficiency is given by

$$\eta_\mathrm{int}^\mathrm{eq}(T) = \frac{I_\mathrm{PL}(T)}{I_0} \tag{4.14}$$

In addition to a decrease in the quantum efficiency, most semiconductors undergo a noticeable narrowing of the band gap with increasing temperature, which manifests itself in a shift of the PL peak position. The band gap narrowing is caused by a larger interatomic spacing as a result of increasing thermal energy. The narrowing can be described phenomenologically by the Varshni equation

$$E(T) = E_0 + \alpha T^2/(\beta + T) \tag{4.15}$$

where α and β are parameters. Monitoring the behavior of the *PL intensity as a function of the excitation intensity* on the other hand allows for determination the origin of near band edge peaks. It is known that the PL data can be well fitted to the power relationship

$$I_{PL}(L) = AL^k \tag{4.16}$$

where L is the excitation intensity and k is the power factor [49]. The underlying recombination process for $1 < k < 2$ is known to be excitonic, whereas for $k < 1$ either a donor state (D-h), an acceptor state (e-A) or both states (donor-acceptor pair transition) are involved.

Time-resolved photoluminescence

Time-resolved photoluminescence (TRPL) is a technique for characterization of carrier lifetimes in semiconductors, and both nanostructures and bulk material can be investigated by this method. In the previous section, it was pointed out that defect states generally trigger non-radiative decay, while radiative decay is due to band-to-band recombination. Naturally, both kinds of recombination take place simultaneously and contribute to the effective lifetime, which is measured by TRPL. In addition, a variety of defects might be present in the crystal, for instance caused by surface states or due to alloying. Therefore, the expression for the carrier lifetime presented in Eq. 4.1 is extended to

$$I(t) = \sum_{n=1}^{x} I_n \exp\left(-t/\tau_n\right) \tag{4.17}$$

where $I(t)$ is the PL intensity at time t, I_n is the initial intensity of the nth component and τ_n the lifetime. A typical TRPL curve exhibiting multi-exponential behavior is shown in Fig. 4.3 (a). For reliable determination of the lifetime from multi-exponential decay curves at each point of time, a variety of methods can be applied. One way is to determine the slope of the tangent to the curve at a characteristic point of time, as illustrated by the turquoise tangent in Fig. 4.3 (a). An alternative method is to calculate the instantaneous lifetime, which is defined by

$$\tau_{\text{inst}}(t) = \frac{-\tau_{\text{PL}}(t)}{d\tau_{\text{PL}}(t)/dt} \tag{4.18}$$

For this purpose, the transients have to be fitted by the sum of a few exponential decay curves prior to the calculation. A calculation with the actual data sets is difficult, since the scatter of the data would lead to positive gradients and thus distort the result. An example of the instantaneous lifetime is presented in Fig. 4.3 (b). In addition, calculating the instantaneous lifetime gives
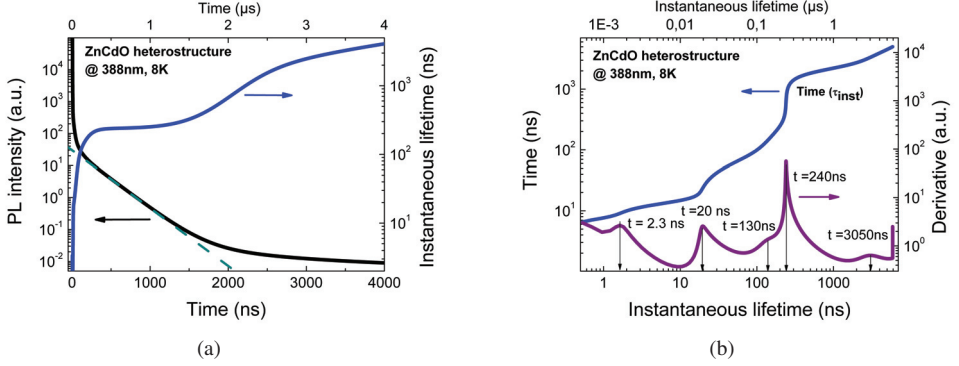
Figure 4.3: *Example for time-resolved PL data and instantaneous lifetime (a) and time against instantaneous lifetime (b), explanation see text.*

insight in the dominant lifetimes. At inflections points on the τ_{inst} curve another process comes into play. Thus, these characteristic lifetimes can be determined by taking the derivative of time(τ_{inst}), as illustrated by the purple curve in Fig. 4.3 (b). However, the precise determination of the lifetimes by either method is challenging. The graphical determination of the lifetime is difficult, if the decay is multi-exponential and thus no clear regimes can be distinguished. The challenge with the instantaneous lifetime is that, if too few exponential decay curves are used to fit the data, the kinks in the curve will represent the number of exponential curves used instead of the number of actual processes in the sample.

A complete study of the lifetimes in a material always involves recording of the temperature dependences of the PL decay curves, as such measurements allow for discrimination of radiative and non-radiative lifetime components, τ_R and τ_{NR}. The calculation of τ_R and τ_{NR} is based on the following equations:

$$\frac{1}{\tau_{\text{PL}}(T)} = \frac{1}{\tau_R(T)} + \frac{1}{\tau_{\text{NR}}(T)} \tag{4.19}$$

$$\eta_{\text{int}}^{\text{eq}}(T) = \frac{1}{1 + \tau_R(T)/\tau_{\text{NR}}(T)} \tag{4.20}$$

Combining Eq. 4.19 and 4.20 yields discrete expressions for τ_R and τ_{NR}, respectively

$$\tau_R(T) = \frac{\tau_{PL}(T)}{\eta_{int}^{eq}(T)} \tag{4.21}$$

$$\tau_{NR}(T) = \frac{\tau_{PL}(T)}{1 - \eta_{int}^{eq}(T)} \tag{4.22}$$

which only depend on the effective lifetime $\tau_{\text{PL}}(T)$ and the internal quantum efficiency $\eta_{\text{int}}^{\text{eq}}(T)$, which can be determined by Eq. 4.14.

4.2   Transmittance and diffuse reflectance spectrophotometry

A standard technique to determine absorption properties of materials are transmittance and diffuse reflectance measurements. In the case of semiconductors, the optical band gap can be estimated, and also discrimination between direct and indirect band gaps is possible [50]. The schematic in Fig. 4.4 illustrates the physical processes during the measurement. The incident light is either absorbed, reflected, scattered or transmitted. The corresponding physical values, the absorptance A, the specular reflectance R, the optical scatter S and the transmittance T, are defined as

$$A \equiv \frac{I_A}{I_0} \qquad R \equiv \frac{I_R}{I_0} \qquad S \equiv \frac{I_S}{I_0} \qquad T \equiv \frac{I_T}{I_0} \tag{4.23}$$

where I_0 is the intensity of the incoming light, and I_A, I_R, I_R and I_T the intensity of the absorbed, reflected, scattered and transmitted light, respectively. As the energy has to be conserved, these values have to sum up to one [51]:

$$1 = A + R + S + T \tag{4.24}$$

As illustrated in the Fig. 4.4, the light can be either specularly or diffusely reflected. In the former case, the angle of reflection equals the angle of incidence. In the latter case, in the presence of dull, scattering surfaces, multiple reflections at surfaces of small particles take place, scattering the incident light in various directions. In addition to the measures introduced above, the optical density (O.D.) is normally used for spectroscopy measurements to describe the extinction properties of a material:

$$O.D. = -ln\frac{I_T}{I_0} = \alpha d \tag{4.25}$$

where d is the thickness of the probed material. The absorption coefficient α is defined by

$$I(z) = I_0 e^{-\alpha z} \tag{4.26}$$

The absorption coefficient can be determined by calculating the transition probability P_{if} between the initially state in the VB and the final state in the CB, which is given by first-order time-
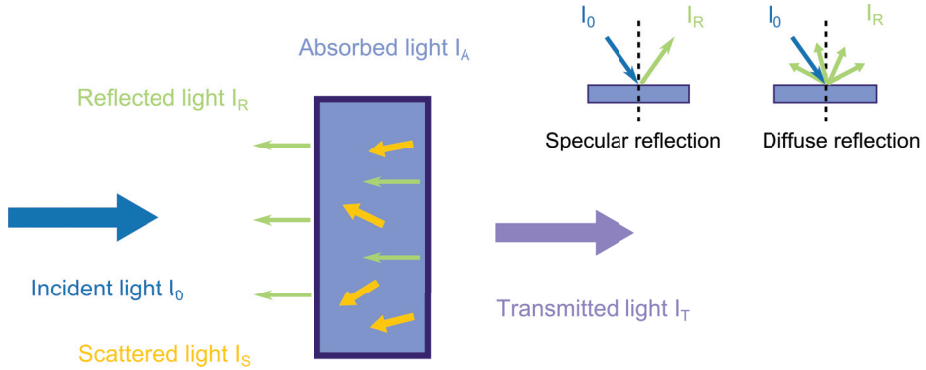
Figure 4.4: *Illustration of interaction of light with a solid.*

dependent perturbation theory [48]:

$$P_{if} = (\frac{2\pi}{h})M_{if}^2 g_n \tag{4.27}$$

M_{if} is the matrix element between the initial and final state of system, i.e. before and after absorption of a photon (and phonon for indirect semiconductors), g_n denotes the density of final states in the CB, which is proportional to $(h\nu - E_g)^{1/2}$ for a parabolic bandstructure. Therewith, the absorption coefficient for direct allowed transitions can be expressed by [52]:

$$\alpha_d^a \sim \frac{(h\nu - E_g)^{1/2}}{h\nu} \tag{4.28}$$

For calculations of the band gap from absorption measurements, α is often given as follows [53]:

$$\alpha_d^a h\nu = const. (h\nu - E_g)^n \tag{4.29}$$

where the power index n denotes the nature of the optical absorption process, $n = 1/2$ indicates direct allowed transition, $n = 3/2$ direct forbidden transition, $n = 2$ indirect allowed transition and $n = 3$ indirect forbidden transition. A common way of presenting transmission data ('Tauc plot') of direct semiconductors is therefore to plot $(\alpha h\nu)^2$ versus $h\nu$ (for indirect semiconductors $(\alpha h\nu)^{1/2}$ is plotted vs $h\nu$). The extrapolation of linear regions in the plot will then lead to an intersection with the x-axis at the energy corresponding to E_g. For wavelengths corresponding to energies smaller than the band gap, absorption is possible via phonon assisted transitions. If

phonon-assisted absorption occurs, a tail (Urbach tail) will be present in the absorption spectra [54].

Diffuse reflectance measurement data are often analyzed following a standard procedure based on the two-flux model of Kubelka and Munk, which describes the absorption and scattering properties in layers. In the special case of an absorbing material of infinite thickness, the relative diffuse reflectance R_∞ can be expressed by [55]:

$$\frac{k}{s} = \frac{(1 - R_\infty)^2}{2R_\infty} \equiv F(R_\infty) \tag{4.30}$$

where k is the (molar) absorption coefficient of the sample and s the scattering coefficient. The relative diffuse reflectance R_∞ is defined by $I_{sample}/I_{standard}$ and $F(R_\infty)$ is the so-called Kubelka-Munk function. Assuming that the light is reflected in a perfectly diffuse manner, $K = 2\alpha$ and Eq. 4.30 reduces to [56]:

$$F(R_\infty)h\nu = \alpha_\mathrm{d}^\mathrm{a}h\nu = const.(h\nu - E_\mathrm{g})^n \tag{4.31}$$

The band gap can thus be determined applying the extrapolation procedure introduced above.

4.3   Voltammetry

Voltammetry is a common method to study chemical reactions and to analyze the chemical composition of samples by monitoring the current as a function of the applied potential [40]. The current-potential curves, the voltammograms, are usually generated by varying the potential and simultaneously measuring the current. In photoelectrochemistry, cyclic voltammetry is used to test the performance of the semiconductor electrode. A typical PEC experimental setup, as schematically illustrated in Fig. 4.5, consists of six primary components, a semiconductor photoanode (photocathode in case of a p-type semiconductor) serving as a working electrode (WE), a counter electrode (CE), a reference electrode (RE), a potentiostat and in addition an electrolyte and a solar simulator. The key unit in the experimental setup is the potentiostat, since it both controls the applied voltage and simultaneously measures the resulting current. For this purpose, the potential of the working electrode against the reference electrode is set to a desired value by the potentiostat, which is achieved by the potentiostat regulating the current between the working electrode and the counter electrode. The aim of the reference electrode is solely to
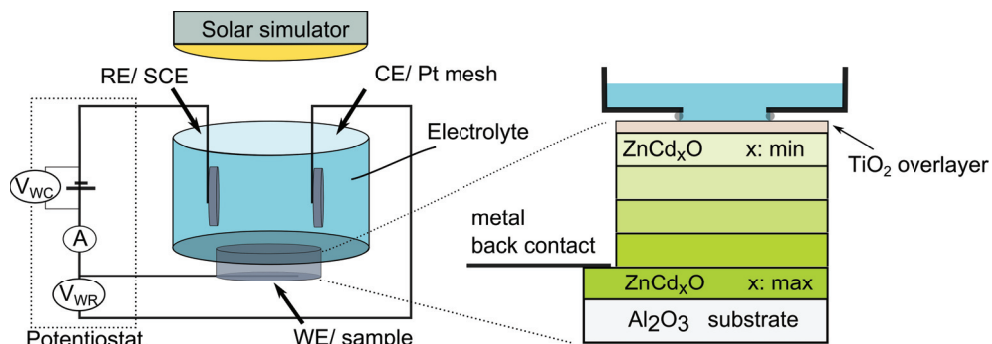
Figure 4.5: *Illustration of a three electrode setup for voltammetry measurement consisting of a counter electrode (CE), a reference electrode (RE) and a working electrode (WE) immersed in electrolyte. The ohmic contact to the WE (here ZnCdO photoanode) is realized by deposition of a metal back contact on the bottom most ZnCdO layer. The potentiostat controls the applied voltage and simultaneously measures the resulting current. The illumination of the sample is controlled by opening/closing a shutter in front of solar simulator.*

serve as a reference point for regulating the voltage of the working electrode at any time and thus, the potentiostat ensures that no current goes through this electrode. In the case of an n-type semiconductor photoelectrode, a characteristic I-V curve is shown in Fig. 4.6 [57]. The black dotted curve depicts the dark current (= no illumination), while the yellow one represents the I-V characteristics under illumination of the cell. For bias below the flatband potential ($E < E_{FB}$, forward bias), the bands bend downwards giving rise to an accumulation layer at the surface of the semiconductor electrode and thus a cathodic (reduction) current across the interface, as illustrated in Fig. 4.6. With increasing bias the net current decreases, since the accumulation layer shrinks and the cathodic and anodic current become equal. At $E = E_{FB}$, there is no current across the interface, since the bands are flat and thus there is no electric field to separate any carriers. For bias above the flatband potential ($E > E_{FB}$, reverse bias), the bands bend upwards and a depletion layer develops at the surface of the semiconductor. Therefore, in the dark, no current flows. Under illumination however, carriers are generated and separated by the electric field, so that an anodic current flows across the interface [57, 58]. In order to study the kinetics in the PEC, the current is measured against time. While the applied bias is constant for this measurement, the illumination is switched on and off. A photoanodic spike is usually observed after the light has been switched on, which flattens out after a certain period of time reaching the stable current value. The cause of the spike is a separation of electron hole pairs at the surface of the semiconductor [59].
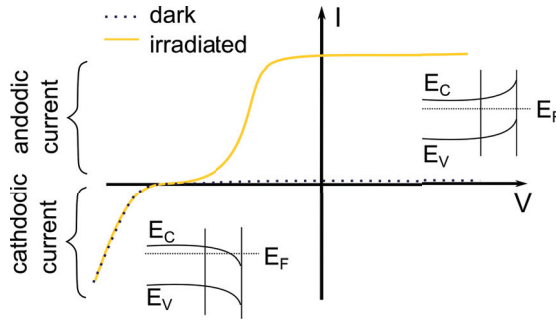
Figure 4.6: *Ideal voltammogram for an n-type photoanode in the dark (dotted line) and under illumination (yellow solid line). For bias $E < E_{\text{FB}}$, the bands bend downwards giving rise to a cathodic current, for $E > E_{\text{FB}}$, the bands bend upwards and an anodic current only flows when carriers are generated by irradiation of the sample. At $E = E_{\text{FB}}$, the bands are flat and thus no current is measured.*

4.4 Rutherford backscattering and time of flight elastic recoil detection analysis

Rutherford backscattering spectrometry (RBS) and time-of-flight elastic recoil detection analysis (Tof-ERDA) are commonly used to gain quantitative information about elemental compositions of surfaces and thin films employing ion beams. In both techniques, a high energy ion beam is accelerated onto the sample and the energy loss, which is due to elastic collisions in the film, is detected (see Fig. 4.7). RBS typically uses light ions, such as ^{4}He, and the energy of the backscattered ions is measured. Their energy E_1 is a function of the scattering angle, the initial energy of the ions and the ratio of the projectile mass M_1 to the target nucleus mass M_2 [60]:

$$E_1 = E_0 \cdot \left(\frac{M_1 \cos\theta_1 \pm \sqrt{M_2^2 - M_1^2(\sin\theta_1)^2}}{M_1 + M_2} \right)^2 \tag{4.32}$$

As E_1 is an unambiguous function of M_2, the elemental composition of the film can be obtained from the energy spectra [61]. RBS is especially suited to detect heavy elements, since the differential cross-section, which describes the probability of observing a scattering event, is proportional to the square of the atomic number of the target atom. Detection of light elements, as for instance Mg, is feasible using Tof-ERDA measurements. This technique utilizes the energy of forward scattered recoil ions to construct an elemental depth profile of the sample. In
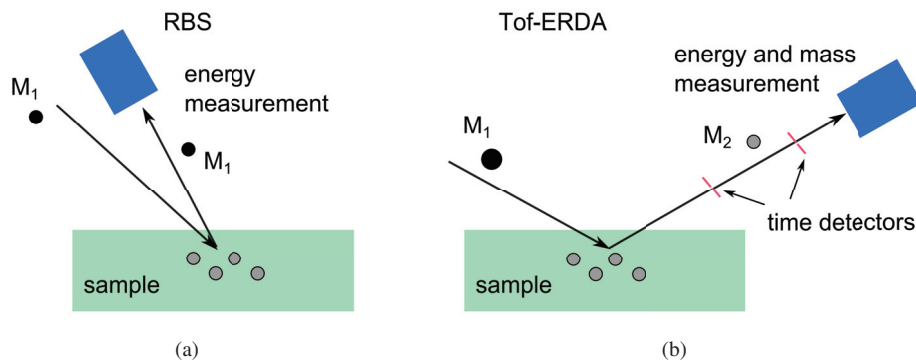
Figure 4.7: *Schemactics of (a) RBS and (b) Tof-ERDA techniques. An ion beam is directed onto the sample and the energy of the backscattered ions (RBS) and the recoil ions (ERDA) is detected, respectively, yielding an elemental depth profile of the sample. Time detectors in the Tof-ERDA setup allow for mass measurement of the recoil ions.*

order to transfer sufficient energy to all kinds of target atoms, heavy projectile ions (^{127}I, ^{197}Au) are employed. The detection of the ions needs a more advanced setup compared to RBS, since not only the energy but also the mass of the recoil ions has to be determined. Among several other spectrometer setups, which are commonly used for ERDA, a time-of-flight detector was employed in the course of this work to analyze the elemental composition of ZnMgO films. As illustrated in Fig. 4.7 (b), when the recoil ions leave the sample, first their mass is determined by time-of-flight spectroscopy accomplished by two timing gates, and second, their energy is measured. The resulting bi-parametric spectra for each of the atomic species (time-of-flight vs. energy of the recoil ions) can subsequently be converted to a depth profile.

4.5 X-ray diffraction analysis

X-ray diffraction (XRD) analysis is a structural characterization technique, where information about the arrangement of atoms and the composition of a material is gained by probing the material with x-rays and detecting the diffracted x-ray patterns [62]. XRD is a commonly used tool for material development and process control, since it is non-destructive and applicable for characterization of both epitaxial films and substrates. Monochromatic, short wavelength x-rays, i.e. electromagnetic radiation with λ in the range of a few Å, are used for XRD. The x-ray source of the Bruker D8 diffractometer employed in this work, is a Cu K$_{\alpha 1}$ line, the wavelength of which
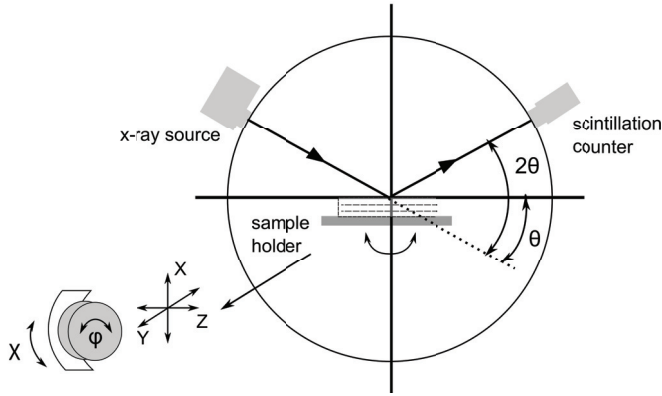
Figure 4.8: *Illustration of the XRD geometry for analysis of thin films: The x-ray beam emitted by the Cu tube is conditioned by a Goebbel mirror and a Ge monochromator. On the secondary side, the diffracted beam is passed through slits and is analyzed by scintillation counters.*

is $\lambda_1 = 1.540594\,\text{Å}$. A schematic of a typical diffractometer geometry is shown in Fig. 4.8. The x-ray beam hits the sample at the angle θ to the surface and the diffracted x-ray intensity is detected by a scintillation counter at the angle 2θ. In order to yield maximal intensity, the sample holder, which is mounted on the cradle, can be adjusted in several directions and angles, as indicated in the schematic. Basic XRD analysis usually includes $2\theta - \theta$ scans, employed for precise measurements of the lattice parameters of the crystal, and rocking curve measurements used to gain information about the film quality. The $2\theta - \theta$ scan is performed by tilting the sample and thus varying the angle of incidence, θ, and simultaneously detecting the scattered intensity I at an angle 2θ, which is varied accordingly with θ. When θ is at the Bragg angle θ_B, which is defined by the Bragg condition for diffraction

$$2d_{hkl} \sin \theta_B = n\lambda \tag{4.33}$$

where d_{hkl} denotes the interplanar spacing and n the order of diffraction, the intensity of the diffracted beam becomes maximal. For hexagonal crystals, as for instance ZnO, the interplanar spacing is given by

$$d_{hkil} = \left(\frac{h^2 + hk + k^2}{3a^2/4} + \frac{l^2}{c^2} \right)^{-1/2} \tag{4.34}$$

and for cubic crystals it is

$$d_{hkl} = \left(\frac{h^2 + k^2 + l^2}{a^2} \right)^{-1/2} \tag{4.35}$$

Rocking curves are obtained by varying θ and measuring I at a fixed angle $2\theta_{fixed}$. The full width at half maximum (FWHM) of the rocking curve is a direct measure for the defect density in the film, since the broadening of the rocking curve is proportional to the square root of the dislocation density.

4.6 Scanning electron microscopy

Scanning electron microscopy (SEM) provides information about the topography of a sample and allows for imaging of areas with different chemical compositions. The images are obtained by focusing an electron beam on the sample and monitoring the interaction of the electrons with the solid [62]. When colliding with electrons of the atomic shell, the primary electrons give off some of their energy and electrons from the atom are excited. The excited electrons themselves undergo inelastic and elastic scattering processes before they escape from the substrate surface. The interaction volume, which depends on the angle of incidence of the electrons as well as on the specimen material, is illustrated in Fig. 4.9. Light elements allow a deeper penetration of the beam, while the scattering volume of heavy elements lies closer to the surface due to stronger scattering. Among several interactions that take place, such as emission of x-rays or Auger electrons, the emission of secondary electrons (SE) and backscattered electrons (BSE) is routinely used in SEM analysis. The secondary electrons, which are generated close to the surface, are employed to image the sample topography. The backscattered electrons give complementary information about different chemical compositions. Depending on the electrons' energy and the sample preparation, resolution in the order of a few nanometers can be achieved by SEM. A column of a SEM tube is shown in Fig. 4.9. The scanning electron beam is collimated and focused on the sample by electromagnetic lenses. An aperture reduces the convergence angle of the beam, before the focused beam is scanned across the sample by the aid of deflection coils. The secondary as well as the backscattered electrons are detected by scintillation detectors.

Some microscopes are additionally equipped with energy dispersive x-ray (EDX) spectroscopy setups, which give further information about the elemental composition of the sample by analyzing the characteristic x-rays, which are due to the interaction of the incident electrons with the atomic-shell electrons. Inner-shell electrons are excited in higher unoccupied states or are
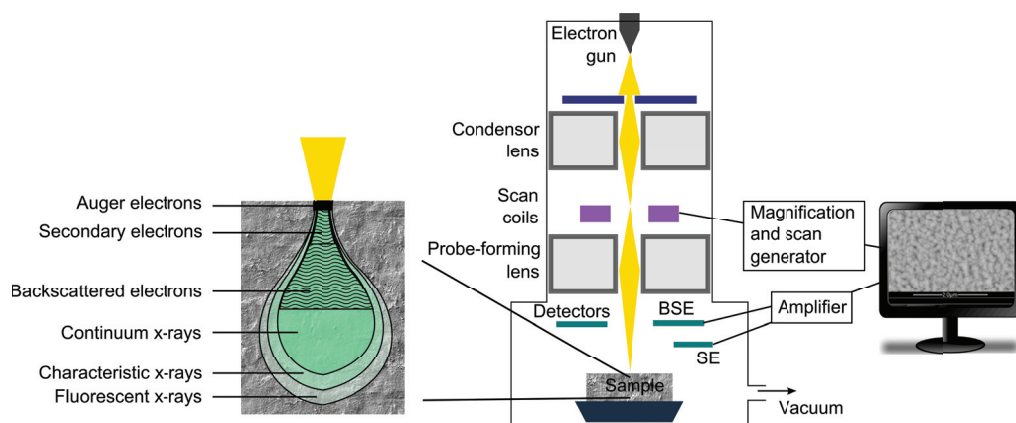
Figure 4.9: *Schematic of a scanning electron microscope and the interaction volume of the electron beam probing the sample. Secondary electrons (SE) and backscattered electrons (BSE) serve as a source of information of the sample topography and contrast between areas with different chemical compositions, respectively. The characteristic x-rays are used for characterization of the elemental composition.*

removed from the atom, given the energy of the primary electrons is at least as high as the relevant binding energy. Going back to its ground state, an electron from the outer shell takes the vacancy in the inner shell. This process is coupled to the emission of either a photon or an Auger electron. Further x-ray emission and electron transitions will continue until the atom reaches its ground state and, thus, the characteristic energy E_c carried by the photons is determined by the energy difference between the higher energy and the lower energy level.

Chapter 5

Results

The following chapter provides a brief description of the performed studies and a summary of the main results and findings attained in the course of this thesis. The first section deals with the nature of the dominating deep level defects observed in ZnMgO. The second section is devoted to the study of carrier dynamics in various ZnCdO structures under the aspect of interface recombination and in-built field-related carrier drift. Finally, the last section focusses on the performance of the ZnCdO photoelectrodes in photoelectrochemical cells.

5.1 Band gap model for deep level defects in ZnMgO

Mastering synthesis of Zn(Cd,Mg)O alloys opens a wide range of promising applications. ZnMgO, having a wider band gap than ZnO, may, for instance, be employed as a barrier layer around active ZnO regions in quantum well structures or used as UV absorber and emitter, respectively. Optically active deep levels are, however, commonly present in ZnMgO alloys due to various defects, including zinc interstitials (Zn_i), zinc vacancies (V_{Zn}), oxygen interstitials (O_i), oxygen vacancies (V_O) and Mg interstitials (Mg_i). The synthesis of defect-free ternary alloys is particularly challenging due to the different crystallographic structures of ZnO and MgO. In order to improve the material properties and thus the performance of possible devices, a thorough understanding of the nature of the defects is imperative, and the aim of this work was to contribute with further knowledge about the origin of deep level defects by correlating optical properties in ZnMgO to certain intrinsic defects.
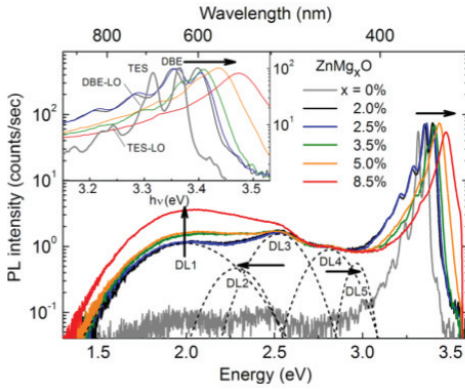
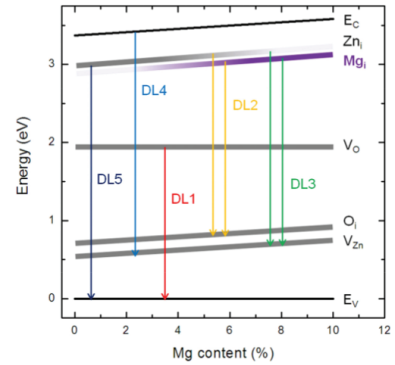**Figure 5.1:** *Low temperature cw PL of ZnMgO mulitlayers with Mg content varying between* 0 *and* 8.5%.

Figure 5.2: *Band gap diagram for ZnMgO explaining the DL emission trends for increasing Mg content presented in Fig. 5.1.*

A series of thin film ZnMgO samples ($d \sim 200\,\text{nm}$), having Mg concentrations ranging between 0 and 8.5%, were therefore synthesized on c-sapphire by MOVPE and examined by PL spectroscopy. The results of this study were published in paper I. In total, five deep level emission bands could be resolved in the PL spectra, shown in Fig. 5.1. Analysis of the observed changes of deep emission bands regarding their peak energy upon Mg doping led to a tentative band gap model for ZnMgO, which is illustrated in Fig. 5.2. The blue bands at 3.0 and 2.8 eV, following the band gap broadening, are associated to free-to-bound type transitions between Zn_i/V_{Zn} with E_V/E_C edges, with the Zn_i level being located at $E_V + 3\,\text{eV}$ and the V_{Zn} level at $E_V + 0.6\,\text{eV}$. The emission energy of the red band at $2\,\text{eV}$ does not follow the blueshift trend with increasing Mg content but approximately holds it position. This trend may be directly explained by assignment of the red band to the V_O donor level, which was assumed to be pinned at $\sim E_C - 1.3\,\text{eV}$. The green bands at 2.3 and 2.5 eV, showing a tendency to red-shift under increasing Mg content, are ascribed transitions between Zn_i donors and V_{Zn} and O_i acceptor states. The red-shift is interpreted by the increasing number of Mg_i and thus competing supply of electrons from slightly deeper Mg_i donor states.

Once a deeper understanding of origin of the deep level bands in ZnMgO had been gained, the knowledge was extended further to the twin ternary alloy ZnCdO. Controlled growth of single film ZnCdO by MOVPE could be achieved [24], making synthesis of ZnCdO-based photoelectrodes and possible:

5.2 ZnCdO heterostructures as photoelectrodes

ZnCdO is a promising alloy for photovoltaic devices, since its band gap can be tuned throughout a wide portion of the visible solar spectrum. A particular application is the use of ZnCdO as a photoelectrode in PECs. The absorption efficiency of the photoelectrode, and therewith of the whole PEC device, may be further increased by stacking several ZnCdO layers with different Cd content. In addition to the enlarged absorption range, the gradually increasing band gap is expected to enhance the charge separation properties in the electrode due to the arising built-in field. The stacking of the single layers may, however, give rise to formation of additional non-radiative recombination sites at the multiple interfaces. Therefore, a general insight into the absorption characteristics and the carrier dynamics in these multilayer structures is essential for device implementations. In this work, the absorbing properties and recombination mechanisms of a variety of Zn(Cd)O single layers and ZnCdO multilayer films were studied by spectropho-tometry and PL spectroscopy (results are published in paper II and partly IV). In addition, in order to address the effect of the multiple interfaces and built-in fields on carrier dynamics, mea-surements were performed on linearly-graded band gap ZnCdO samples, where the Cd content increased linearly in contrast to the step-graded band gap ZnCdO multilayers samples (presented in paper III). The studies on optical properties of the samples were accomplished by demonstra-tion of photoelectrochemical activity of the proposed ZnCdO multilayer electrode by means of voltammetry (paper IV).

5.2.1 Optical activity and carrier dynamics in graded band gap ZnCdO structures

The light absorption and excitonic emission in a wide spectral range could be observed by absorp-tion and low temperature cw PL measurements, respectively (Fig. 5.3 and 5.4). The broadened emission band for multilayer structures compared to single films was explained by combined band-edge emission for the individual layers. In fact, the multilayer structures exhibited a unique carrier distribution, where the carrier generation peaks deep inside the sample compared to a uniform ZnO film of the same thickness, where the number of generated carriers decreases with absorption depth.

The carrier dynamics in the ZnCdO heterostructure were investigated in detail by means of time-resolved PL. The measurements revealed that the carrier recombination processes have multi-
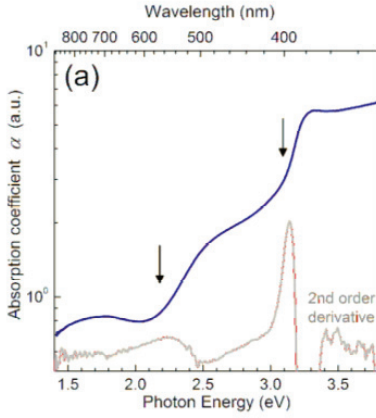
Figure 5.3: *Absorption spectrum of a ZnCdO mulitlayer revealing multiple absorption edges.*
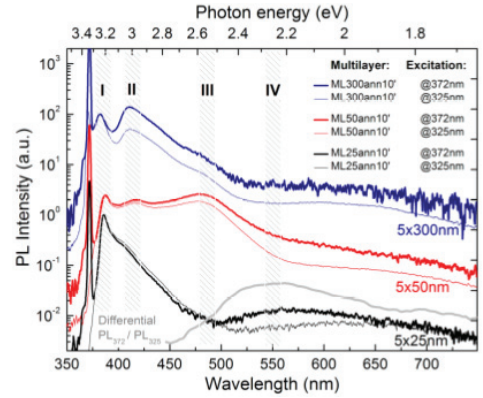

Figure 5.4: *PL spectra of ZnCdO mulitlayers obtained at 10 K.*
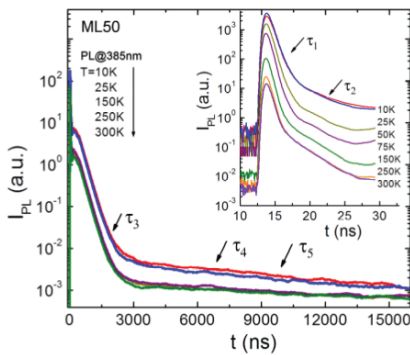
Figure 5.5: *Typical transients in ZnCdO MLs revealing multi-exponential decay. The fast decay components, shown in the inset, are in the order of a few nanoseconds, the slowest decay component is in the order of a few microseconds.*

Figure 5.6: *Temperature dependencies of PL lifetime τ_{PL} with the corresponding radiative and non-radiative lifetime components. Above the transition temperature, T_{TR} non-radiative recombination processes dominate. The inset show the T_{TR} trends in different thick MLs.*

Table 5.1: *Depth-resolved lifetime parameters (ns) in linearly graded, step-graded and flat bandgap ZnCd$_x$O structures as determined by TRPL measurements at 1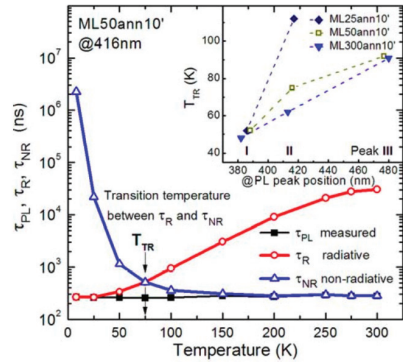0K. The values presented in parenthesis are upon annealing at $800\,^\circ$C for 10 minutes. Arrow symbols indicate mutual orientation of carrier drift and diffusion vectors, E and D, for each case. Labels L-H and H-L stand for low-high $(0 - 60\%)$ and high-low $(60 - 0\%)$ linear variation of Cd, ML - multilayer stack with $0/5/10/40/60\%$ of Cd, SL - single layer with fixed Cd content.*

Sample	$\mathbf{E \parallel D}$	Surface		Bulk	Interface	
		ZnO-like	CdO-like		CdO-like	CdO-like
L-H $(0 - 60\%$ Cd$)$	↑↑	0.23 (0.10)		0.20 (0.40)		0.17 (0.12)
L-H $(0 - 60\%$ Cd$)$	↑↓	0.40 (0.14)		0.27 (0.41)		0.10 (0.10)
H-L $(60 - 0\%$ Cd$)$	↑↑		0.11 (0.10)	0.17 (0.33)	0.27 (0.14)	
H-L $(60 - 0\%$ Cd$)$	↑↓		0.11 (0.10)	0.11 (0.44)	0.17 (0.22)	
ML $(0/5/10/40/60\%$ Cd$)$	↑↑	0.44 (0.25)		0.48 (0.50)		(1.60)
ML $(0/5/10/40/60\%$ Cd$)$	↑↓	(0.25)		0.90 (0.90)		(1.60)
SL $(0\%$ Cd$)$		0.44 (0.34)		0.44 (0.44)		
SL $(5\%$ Cd$)$		0.44 (0.42)		0.44 (0.44)		

exponential character with up to five lifetime components. An example of typical mulitexponential transients is depicted in Fig. 5.5. The measured PL decay time constants (τ_{PL}) ranged between less then a nanosecond and a few microseconds and result from contributions of several recombination processes. The decay time constant τ_{PL} was resolved into its radiative (τ_{R}) and non-radiative (τ_{NR}) lifetime components by a procedure analyzing the temperature behavior of τ_{PL} and of the quantum efficiency $\eta(T)$ to understand to which extend non-radiative processes were competing with the radiative processes. The transition temperature T_{TR} was introduced as an auxiliary parameter to describe the transition of predominately radiative to non-radiative recombination. Thus, a lowered T_{TR} corresponds to an increased contribution from non-radiative recombinations. Figure 5.6 illustrates the concept of τ_{R}, τ_{NR} and T_{TR} by using the example a typical step-graded band gap ZnCdO structure. Measurements performed at various probing wavelengths, which can be correlated to different single ZnCdO layers in the multilayer stack, show that T_{TR} is lowest at the top layer of the structure. In addition, a general decrease of the long decay times was observed with decreasing probing wavelengths, i.e. closer to the surface. These observations led to the conclusion that non-radiative processes play a more dominant role in the top-layer of the heterostructure. The non-radiative lifetime at room temperature as well as the internal quantum efficiency are generally lower in the step-graded multilayer films com-

pared to the single layer films (0.77% versus 1.5%) indicating a higher density of non-radiative recombination centers. The nature of the non-radiative recombination centers was assessed by comparing lifetime parameters in a variety of heterostructures with different geometries. The systematic analysis of lifetime parameters in single layer films, step-graded and linearly-graded band gap ZnCdO structures led to the conclusion that higher non-radiative recombination losses and correspondingly shorter carrier lifetime (summarized in table 5.1), are mostly due to inferior crystallinity of material with higher Cd content.

5.2.2 Photoelectrochemical testing

The optical measurements, showing optical activity in each of the single layers in the ZnCdO heterostructures, were accomplished by testing the performance of the same structures in a PEC. As ZnO dissolves in most electrolytes, applying an anticorrsion layer is imperative. In this work, TiO_2 was chosen to be deposited on the ZnCdO anodes to prevent the photoelectrode from dissolution during photoelectrochemical measurements. The thickness of the films, prepared by atomic layer deposition and pulsed layer deposition, ranged between $5 - 50\,nm$. In the measurements, which were performed both under AM1.5 and AM0 illumination, the highest photocurrent intensity was achieved under the UV-rich illumination leading to the conclusion that the pure ZnO layer may play a dominating role in the multilayer photoanode. Photoanodic spikes in the photocurrent, observed after exposure to light (Fig. 5.7), indicate the presence of recombination centers, as also concluded from time-resolved PL measurements. The increase of the photocurrent for decreasing protective layer thickness, the lack of saturation current in J-V measurements (see Fig. 5.8) and change of surface morphology seen by SEM after exposure to the electrolyte, suggest that corrosion processes occur during the photoelectrochemical measurements despite the protective film.
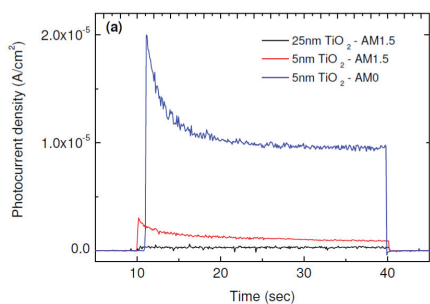
Figure 5.7: *Kinetic behavior for ZnCdO electrodes with TiO$_2$ protective films measured under AM1.5 and AM0.*
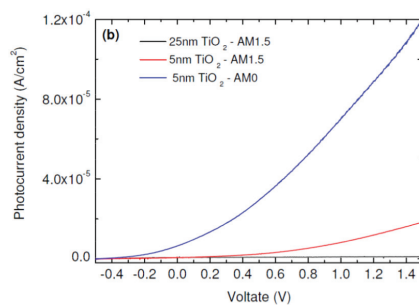
Figure 5.8: *J-V curves for ZnCdO electrodes with TiO$_2$ protective films measured under AM1.5 and AM0.*

Chapter 6

Concluding remarks

The aim of this thesis was to contribute to a deeper understanding of ZnO ternary alloys and to explore novel ZnO-based heterostructures for photovoltaic applications. The first part of the thesis was devoted to the study the nature of defect-related luminescence in ZnMgO thin films. The optically active deep levels of the samples were investigated by temperature dependent PL spectroscopy. The PL spectra of the samples studied had Mg contents ranging from 0% to 8.5%, which lead to a gradual band gap broadening. Based on the changes of the peak positions of the deep band emission, which were observed with increasing Mg content, a band gap model for ZnMgO could be attained. In summary, the two bands around $2.4\,\mathrm{eV}$, which were assigned to acceptor-donor pair transitions involving Zn_i donors, showed a redshift with increasing Mg content. The observed shift was interpreted as an increasing contribution of electrons from Mg_i donor state, which is located slightly deeper than Zn_i state. The band at $2.0\,\mathrm{eV}$, which showed no apparent shift in this study, was associated with oxygen vacancies. The bands at 3.0 and $2.8\,\mathrm{eV}$, were assigned to free-to-bound type transitions from the Zn_i band to the the valence band edge and transitions from the conduction band edge to the V_{Zn} band, respectively. The assignments of deep level PL bands to different native defects and the resulting band gap model for ZnMgO, which was attained in this study, has contributed to a better understanding of the origin of defect-related luminescence in ZnMgO, but further studies should be pursued to validate the proposed assignment. As annealing in different atmospheres will influence the defect levels in samples, some effort should be put into annealing studies of ZnMgO, comprising both annealing in Zn-, Mg- and O-rich ambients. At the same time, these annealing studies could result in processing routines allowing to control the concentration of defect in the crystals. An alternative way to confirm the proposed model relies on involvement of complementary characterization methods capable of providing an insight into the origin of deep defects. Among suitable techniques

for this purpose are, for instance, deep level transient spectroscopy (DLTS), positron annihilation spectroscopy (PAS) and catholuminescence (CL). Finally, a systematic study of alloys with variable, high Mg content would shed more light on the role of Mg interstitials on optical and electrical properties.

In the second part of this work, a concept of a graded band gap ZnCdO multilayer structure was investigated with regard to photoelectrochemical applications. Optical measurements, which were mainly presented in paper II and IV, showed an enlarged optical emission in ZnCdO multilayers compared to single film ZnO. PL spectroscopy gave clear evidence that the multiple emission components forming a characteristic broad band have excitonic origin. The dynamic processes of the excitonic transitions, which were studied in an extended time scale by time-resolved PL and were presented in paper II and manuscript III, were characterized by multi-exponential behavior. In addition, the optical activity of the multilayer structures could be confirmed by photoelectrochemical measurements (summarized in paper IV) providing a proof of concept for the proposed application of ZnCdO multilayers as photoanodes in photoelectrochemical cells. However, both PL spectroscopy and photoelectrochemical analysis show evidence for increased non-radiative recombination in these structures as compared to single layer films. Furthermore, during photoelectrochemical testing of the samples, there were signs of photocorrosion meaning that the thin TiO_2 protective layers, which were deposited on the surface of the ZnCdO structures, were insufficient in preventing the ZnCdO photoanode from corrosion. As the studies proved optical activity and photoelectrochemical response of the ZnCdO, further improvement of the ZnCdO mulitlayer photoanode is well-motivated. Further studies should be dedicated to the optimization of the TiO_2 anti-corrosion layer. A similar photoanode concept using cuprous oxide as a photoanode has been suggested, and in this study corrosion of the active layer could be achieved by deposition of nanolayers of Al-doped ZnO and TiO_2 [43]. As the overlayer is based on ZnO, the proposed oxide structure could also be suitable for the ZnCdO anode. With regard to carrier recombination at the surface and the multiple interfaces, some effort should be put into optimization of the synthesis process. Furthermore, nanostructuring of the photoanode, and therewith increasing the surface of the multilayers, could increase the efficiency of the anodes. In addition, a higher photocurrent in the device could possibly be achieved by optimizing the ohmic contact between the metal electrode and the ZnCdO photoanode in the photoelectrochemical cell. Here, replacing the sapphire substrate by a conducting substrate could be an alternative.

Bibliography

[1] Bose, B. Global warming: Energy, environmental pollution, and the impact of power electronics. *Industrial Electronics Magazine, IEEE* **4**, 6 –17 (2010).

[2] Zobaa, A. F. & Bose, B. K. Renewable energy, global warming problem and impact of power electronics. ICREPQ'11, Gran Canaria, Spain (2011).

[3] Bose, B. Power electronics and motor drives recent progress and perspective. *Industrial Electronics, IEEE Transactions on* **56**, 581 –588 (2009).

[4] Klingshirn, C. *et al.* 65 years of ZnO research – old and very recent results. *physica status solidi (b)* **247**, 1424–1447 (2010).

[5] Koike, K. *et al.* Piezoelectric carrier confinement by lattice mismatch at $ZnO/Zn_{0.6}Mg_{0.4}O$ heterointerface. *Japanese Journal of Applied Physics* **43**, L1372–L1375 (2004).

[6] Currao, A. Photoelectrochemical water splitting. *Chimia* **61**, 815–819 (2007).

[7] Bak, T., Nowotny, J., Rekas, M. & Sorrell, C. Photo-electrochemical hydrogen generation from water using solar energy. Materials-related aspects. *International Journal of Hydrogen Energy* **27**, 991 – 1022 (2002).

[8] Look, D. C. & Claflin, B. P-type doping and devices based on ZnO. *physica status solidi (b)* **241**, 624–630 (2004).

[9] Sun, C. W. *et al.* Optical and electrical properties of $Zn_{1-x}Cd_xO$ films grown on Si substrates by reactive radio-frequency magnetron sputtering. *Applied Physics Letters* **89**, 181923 (2006).

[10] Klingshirn, C., Meyer, B., Waag, A., Hoffmann, A. & Geurts, J. *Zinc Oxide: From Fundamental Properties Towards Novel Applications*, vol. 120 (Springer Series in Materials Science, 2010).

[11] Kim, S.-K., Jeong, S.-Y. & Cho, C.-R. Structural reconstruction of hexagonal to cubic ZnO films on Pt/Ti/SiO$_2$/Si substrate by annealing. *Applied Physics Letters* **82**, 562–564 (2003).

[12] Authors & editors of the volumes III/17B-22A-41B. Zinc oxide (ZnO) distances, ionic radii, further lattice parameters. In O. Madelung, M. S., U. Rössler (ed.) *Landolt-Börnstein - Group III Condensed Matter Numerical Data and Functional Relationships in Science and Technology*, vol. 41B: II-VI and I-VII Compounds; Semimagnetic Compounds (Springer, 1999).

[13] Triboulet, R. & Perrière, J. Epitaxial growth of ZnO films. *Progress in Crystal Growth and Characterization of Materials* **47**, 65 – 138 (2003).

[14] Venkatachalapathy, V. *ZnO and ZnCdO metal organic vapor phase epitaxy: epitaxy, defects and band gap engineering*. Ph.D. thesis, University of Oslo (2011).

[15] Mang, A., Reimann, K. & Rübenacke, S. Band gaps, crystal-field splitting, spin-orbit coupling, and exciton binding energies in ZnO under hydrostatic pressure. *Solid State Communications* **94**, 251 – 254 (1995).

[16] Özgür, Ü. *et al.* A comprehensive review of ZnO materials and devices. *Journal of Applied Physics* **98**, 041301 (2005).

[17] Janotti, A., Segev, D. & Van de Walle, C. G. Effects of cation d states on the structural and electronic properties of III-nitride and II-oxide wide-band-gap semiconductors. *Phys. Rev. B* **74**, 045202 (2006).

[18] Klingshirn, C. ZnO: From basics towards applications. *physica status solidi (b)* **244**, 3027–3073 (2007).

[19] Takeuchi, I. *et al.* Monolithic multichannel ultraviolet detector arrays and continuous phase evolution in Mg$_x$Zn$_{1-x}$O composition spreads. *Journal of Applied Physics* **94**, 7336–7340 (2003).

[20] Segnit, E. R. & Holland, A. E. The system MgO-ZnO-SiO$_2$. *Journal of the American Ceramic Society* **48**, 409–413 (1965).

[21] Chen, J., Shen, W. Z., Chen, N. B., Qiu, D. J. & Wu, H. Z. The study of composition non-uniformity in ternary MgZnO thin films. *Journal of Physics: Condensed Matter* **15**, L475 (2003).

[22] Makino, T. *et al.* Radiative and nonradiative recombination processes in lattice-matched (Cd,Zn)O/(Mg,Zn)O multiquantum wells. *Applied Physics Letters* **77**, 1632 (2000).

[23] Ishihara, J., Nakamura, A., Shigemori, S., Aoki, T. & Temmyo, J. $Zn_{1-x}Cd_x$o systems with visible band gaps. *Applied Physics Letters* **89**, 091914 (2006).

[24] Venkatachalapathy, V. *et al.* Understanding phase separation in ZnCdO by a combination of structural and optical analysis. *Phys. Rev. B* **83**, 125315 (2011).

[25] McCluskey, M. D. & Jokela, S. J. Defects in ZnO. *Journal of Applied Physics* **106**, 071101 (2009).

[26] Vlasenko, L. S. & Watkins, G. D. Optical detection of electron paramagnetic resonance in room-temperature electron-irradiated ZnO. *Phys. Rev. B* **71**, 125210 (2005).

[27] Janotti, A. & Van de Walle, C. G. Native point defects in ZnO. *Phys. Rev. B* **76**, 165202– (2007).

[28] Yuming, S. *et al.* A FP-LMTO study on the native shallow donor in ZnO. *Journal of Electron Spectroscopy and Related Phenomena* **114-116**, 1123–1125 (2001).

[29] Ahn, C. H., Kim, Y. Y., Kim, D. C., Mohanta, S. K. & Cho, H. K. A comparative analysis of deep level emission in ZnO layers deposited by various methods. *Journal of Applied Physics* **105**, 013502–013502–5 (2009).

[30] Bylander, E. G. Surface effects on the low-energy cathodoluminescence of zinc oxide. *Journal of Applied Physics* **49**, 1188–1195 (1978).

[31] Hu, J. & Pan, B. C. Electronic structures of defects in ZnO: hybrid density functional studies. *J. Chem. Phys.* **129**, 154706–8 (2008).

[32] Reshchikov, M. A., Xie, J. Q., Hertog, B. & Osinsky, A. Yellow luminescence in ZnO layers grown on sapphire. *J. Appl. Phys.* **103**, 103514–8 (2008).

[33] Khanna, V. K. Physical understanding and technological control of carrier lifetimes in semiconductor materials and devices: A critique of conceptual development, state of the art and applications. *Progress in Quantum Electronics* **29**, 59 – 163 (2005).

[34] Lagarde, D. *et al.* Exciton and hole spin dynamics in ZnO investigated by time-resolved photoluminescence experiments. *Phys. Rev. B* **78**, 033203 (2008).

[35] Reynolds, D. C. *et al.* Time-resolved photoluminescence lifetime measurements of the Gamma$_5$ and Gamma$_6$ free excitons in zno. *Journal of Applied Physics* **88**, 2152–2153 (2000).

[36] Koida, T. *et al.* Correlation between the photoluminescence lifetime and defect density in bulk and epitaxial ZnO. *Applied Physics Letters* **82**, 532–534 (2003).

[37] Chichibu, S. F. *et al.* Improvements in quantum efficiency of excitonic emissions in ZnO epilayers by the elimination of point defects. *Journal of Applied Physics* **99**, 093505 (2006).

[38] Kubota, M. *et al.* Recombination dynamics of excitons in $Mg_{0.11}Zn_{0.89}O$ alloy films grown using the high-temperature-annealed self-buffer layer by laser-assisted molecular-beam epitaxy. *Applied Physics Letters* **90**, 141903 (2007).

[39] Buyanova, I. A. *et al.* Mechanism for radiative recombination in ZnCdO alloys. *Applied Physics Letters* **90**, 261907 (2007).

[40] Van De Krol, R. & Grätzel, M. *Photoelectrochemical Hydrogen Production*, vol. 102 (Springer Verlag, 2011).

[41] Fujishima, A. & Honda, K. Electrochemical photolysis of water at a semiconductor electrode. *Nature* **238**, 37–38 (1972).

[42] Lindgren, T. *In Search of the Holy Grail of Photoelectrochemistry*. Ph.D. thesis, Uppsala University (2004).

[43] Paracchino, A., Laporte, V., Sivula, K., Grätzel, M. & Thimsen, E. Highly active oxide photocathode for photoelectrochemical water reduction. *Nat Mater* **10**, 456–461 (2011).

[44] H. Schoenmakers, G., Vanmaekelbergh, D. & J. Kelly, J. The mechanism of current-doubling reactions at ZnO photoanodes. *J. Chem. Soc., Faraday Trans.* **93**, 1127–1132 (1997).

[45] Morisaki, H., Watanabe, T., Iwase, M. & Yazawa, K. Photoelectrolysis of water with TiO$_2$-covered solar-cell electrodes. *Applied Physics Letters* **29**, 338–340 (1976).

[46] Zhao, G., Song, B., Han, G., Kozuka, H. & Yoko, T. Graded bandgap semiconductor thin film photoelectrodes. *Chinese Science Bulletin* **46**, 914–917 (2001).

[47] Green, M. A. Do built-in fields improve solar cell performance? *Progress in Photovoltaics: Research and Applications* **17**, 57–66 (2009).

[48] Li, S. S. *Semiconductor Physical Electronics*, vol. 120 (Springer New York, 1993).

[49] Fonoberov, V. A., Alim, K. A., Balandin, A. A., Xiu, F. & Liu, J. Photoluminescence investigation of the carrier recombination processes in ZnO quantum dots and nanocrystals. *Phys. Rev. B* **73**, 165317 (2006).

[50] Murphy, A. Band-gap determination from diffuse reflectance measurements of semiconductor films, and application to photoelectrochemical water-splitting. *Solar Energy Materials and Solar Cells* **91**, 1326 – 1337 (2007).

[51] Stenzel, O. *The Physics of Thin Film Optical Spectra - An Introduction*, vol. 44 (Springer Series in Surface Sciences, 2005).

[52] Yu, P. Y. & Cardona, M. *Fundamentals of semiconductors: physics and materials properties* (Springer Verlag, 2010).

[53] López, R. & Gómez, R. Band-gap energy estimation from diffuse reflectance measurements on sol–gel and commercial TiO_2: a comparative study. *Journal of Sol-Gel Science and Technology* 1–7 (2012).

[54] Schubert, E. F. *Light-Emitting Diodes* (Cambridge University Press, 2006).

[55] Kortüm, G., Braun, W. & Herzog, G. Principles and techniques of diffuse-reflectance spectroscopy. *Angewandte Chemie International Edition in English* **2**, 333–341 (1963).

[56] Morales, A., Mora, E. & Pal, U. Use of diffuse reflectance spectroscopy for optical characterization of un-supported nanostructures. *Revista Mexicana de Fisica S* **53**, 18 (2007).

[57] Bott, A. W. Electrochemistry of semiconductors. *Current Separations* **17**, 87–91 (1998).

[58] Rajeshwar, K. *Fundamentals of Semiconductor Electrochemistry and Photoelectrochemistry* (Wiley-VCH Verlag GmbH & Co. KGaA, 2007).

[59] Radecka, M., Rekas, M., Trenczek-Zajac, A. & Zakrzewska, K. Importance of the band gap energy and flat band potential for application of modified TiO_2 photoanodes in water photolysis. *Journal of Power Sources* **181**, 46 – 55 (2008).

[60] Oura, K., Lifshits, V. G., Saranin, A. A., Zotov, A. & Katayama, M. *Surface science* (Springer, 2003).

[61] Döbeli, M. Characterization of oxide films by MeV ion beam techniques. *Journal of Physics: Condensed Matter* **20**, 264010 (2008).

[62] Ayers, J. E. *Heteroepitaxy of semiconductors* (CRC Press, 2007).

Paper I

Deep level related photoluminescence in ZnMgO

M. Trunk, V. Venkatachalapathy, A. Galeckas, and A. Yu. Kuznetsov

Deep level related photoluminescence in ZnMgO

M. Trunk,[a] V. Venkatachalapathy, A. Galeckas, and A. Yu. Kuznetsov
Department of Physics/Center for Materials Science and Nanotechnology, University of Oslo,
P.O. Box 1048 Blindern, N-0316 Oslo, Norway

Optically active deep levels were investigated in ZnMgO layers using temperature dependent photoluminescence. The samples, grown on *c*-plane sapphire by metal-organic vapor phase epitaxy, exhibited Mg contents ranging from 0% to 8.5% leading to a gradual band gap broadening. The deep level luminescence was found to consist of several emission components centered at 2, 2.3, 2.5, 2.8, and 3 eV. With increasing Mg concentration, the bands at 2.8 and 3eV were found to blueshift, the bands at 2.3 and 2.5eV redshift, while the band at 2 eV holds its position. A model is suggested explaining the deep level luminescence shift trends in terms of interaction of native Zn and O sublattice defects with the introduced Mg interstitials. © *2010 American Institute of Physics.*
[doi:10.1063/1.3518480]

The development of solid-state optoelectronic devices in the uv range has lead to great interest in wide band gap semiconducting materials over the past years. Due to its outstanding optical properties, ZnO is widely considered as a possible alternative to GaN.[1] However, the implementation of ZnO-based devices strongly depends on the progress in mastering band gap engineering and *p*-type doping. Indeed, by mixing ZnO ($E_g \simeq 3.37$ eV) with MgO ($E_g \sim 7.8$ eV) in a controlled way, the band gap of ZnMgO alloys can be tuned allowing for optoelectronic applications in the deep uv and also for fabrication of hetero- and quantum-well structures, high electron mobility transistors, etc. To date, several groups have reported promising results on realization of *p*-type doping in ZnMgO.[2,3] Still, certain complications in fabrication of single phase ZnMgO alloys may arise considering the fact that ZnO crystallizes in wurtzite lattice whereas MgO exhibits rock-salt structure. Furthermore, the solubility of Mg ions in a ZnO lattice was estimated to be 4%,[4] and therefore Mg interstitials are likely to be generated in metastable alloys with higher Mg content. Large amounts of point defects may have detrimental effects on the optical properties and the performance of ZnMgO devices. These issues are well known for ZnO, for which the intrinsic defects have been extensively studied along with considerable attempts to correlate photoluminescence (PL) features with certain deep levels (DL) in the band gap. Nonetheless, a consensus on the DL assignment has not been reached yet. Indeed, while the blue PL band around 3 eV is accordingly associated with zinc interstitials (Zn_i), the contributions from other native defects, such as zinc vacancies (V_{Zn}), oxygen interstitials (O_i), and oxygen vacancies (V_O), remain controversial.[5] Concurrently, there are only few reports on defect-related PL in ZnMgO and, to our knowledge, the effects of Mg doping have not been considered to explain the developments of the DL emission (DLE). In this work, we report on a systematic study of the DLE in ZnMgO alloys with variable Mg contents and propose a model correlating PL features with specific intrinsic defects.

ZnMgO layers were epitaxially grown on *c*-Al$_2$O$_3$ by metalorganic vapor phase epitaxy at 370 °C, at atmospheric

pressure for 60 min resulting in a film thickness of ~200 nm. The composition of the samples was analyzed by time-of-flight elastic recoil detection analysis, while the single phase wurtzite character of the films was confirmed by x-ray diffraction. The samples exhibited Mg contents from 0% to 8.5%. PL was investigated by exciting the films with a 325 nm line of a cw He–Cd laser (10 mW) and analyzing the emitted light by fiber optic spectrometers. The measurements were performed in the temperature range from 10 to 300 K.

Figure 1 shows the PL spectra of the ZnMgO films taken at 10 K. In view of the fact that we focus primarily on development of DLE bands upon Mg doping, all spectra are normalized with respect to one of the characteristic DL bands at 2.8 eV. For comparison, a reference spectrum taken from a pure ZnO sample is also included in Fig. 1, revealing an obvious blueshift of the near band edge (NBE) emission from 3.37 eV (pure ZnO) up to 3.47 eV (Mg 8.5%). Further comparison of ZnMgO and ZnO spectra in the inset of Fig. 1 also shows general broadening of ZnMgO spectral lines, which are the signs of deteriorating crystal quality because of the alloying. Indeed for Mg contents up to 3.5%, spectra from alloy films resemble those from ZnO, showing several
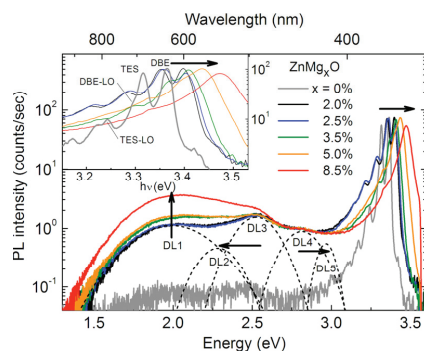

FIG. 1. (Color online) PL spectra taken from ZnMgO at 10 K; arrows indicate the peak shift trends with increasing Mg content while peaks are identified by labels. Assignments for ZnO in the inset correspond to donor bound excitons (DBE), DBE two electron satellite (TES), and their LO phonon replicas (DBE/TES-LO) (Ref. 6).
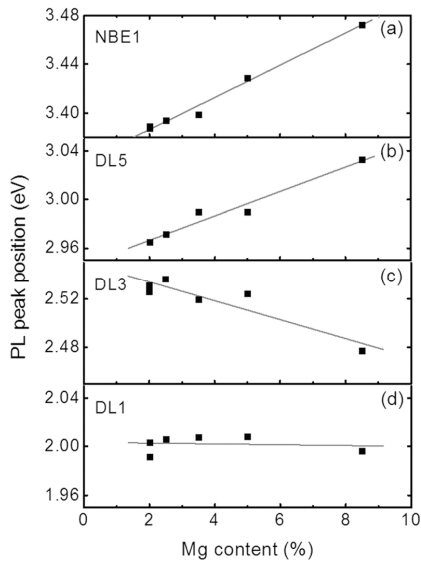
[a]Electronic mail: mareike.trunk@smn.uio.no.

FIG. 2. Energy shifts of characteristic DL and NBE peaks as a function of Mg content.

FIG. 3. (Color online) Schematics of deep levels and corresponding PL transitions for ZnMgO with variable Mg content.

distinct peaks associated with excitonic transitions. For Mg concentrations above 3.5%, the two high-energy peaks merge, and the features in the low energy tails become less pronounced. As a result of alloying, the overall quantum efficiency in ZnMgO films decreases by nearly an order of magnitude.

The increasing Mg concentration also affects the deep level emission (DLE) region of the spectra (see Fig. 1). The broad luminescence band between 1.5 and 3.0 eV was deconvoluted into several Gaussian components in order to resolve individual constituents of the DLE. A set of at least five Gaussian curves was needed to satisfactorily fit the data. The resolved bands are centered at around 2, 2.3, 2.5, and 2.8 as well as 3 eV and are accordingly labeled as DL1–DL5. For all Mg contents, the spectral position of the red DL1 emission band remains centered at 2 eV. The DL2 and DL3 bands are apparently redshifted with increasing Mg content, whereas the higher energy DL4 and DL5 bands exhibit blueshifts. Figure 2 summarizes the observed trends for the NBE, DL1, DL3, and DL5 peak position shifts as a function of the Mg content.

Some of the above mentioned DLE features in ZnMgO have also been observed by other groups.[7,8] Fujihara *et al.*[8] reported both a green (2.50 eV) and a yellow band (2.36 eV) in a series of ZnMgO thin films annealed in various atmospheres. Interestingly, the yellow band was observed to redshift in response to the Mg doping what agrees well with our results. According to investigations by Wu *et al.*,[9] these green and yellow bands are assigned to a recombination of electrons from the conduction band with holes trapped at the V_O and O_i, respectively. Li *et al.*[7] also reported visible emission at around 2.38 eV and attributed it to oxygen defects or impurity levels. However, changes in the band position were not observed upon introduction of Mg into the films.

It should be noted that the incorporation of Mg also affects the intensity of the various DL bands to a different
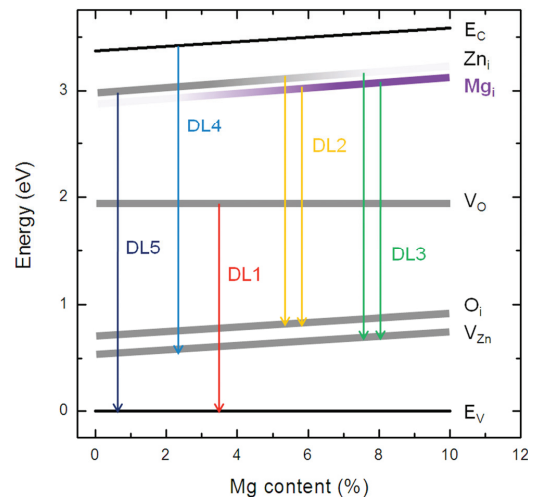
extent, e.g., a considerable increase of the DL1 yield is observed upon increasing Mg content, whereas the DL3 band builds up only a little (see Fig. 1).

In order to assess possible effects of variable Mg concentration in $Zn_{1-x}Mg_xO$, it may be helpful to refer to its electronic structure. If Mg atoms are introduced into the ZnO lattice by substituting Zn atoms, Mg 3s-like states would effectively lift the conduction band (E_C) position, leaving in the first approximation the valence band (E_V) position unaffected. This first assumption in our model of the DLE origin in ZnMgO is included in a schematic of the band gap diagram in Fig. 3. Note that the NBE blueshift seen in Fig. 2(a) is a direct outcome of the band gap broadening. For further assignment of the multiple DLE signatures, we account for optically active native defects in ZnO and the way they can be disturbed by the introduction of Mg in the form of interstitials (Mg_i), vacancies (V_{Mg}), or antisites (Mg_O). This general case can be simplified essentially, taking into account that V_{Mg} can be equally considered as V_{Zn}, whereas Mg_O is likely to have a high formation energy similarly to Zn_O,[1] thus leaving only Mg_i in addition to native ZnO defects for further consideration.

Theoretical calculations of the Zn_i electronic structure[1,10,11] predict a shallow donor behavior, which is in good agreement with luminescence experiments.[12,13] Indeed, the introduction of donor states around E_V+3 eV, coming from Zn_i and other shallow background donors, allows for optical transitions of electrons from this level to E_V, giving rise to the DL5 band (see Fig. 3). The formation of V_{Zn}, on the other hand, yields shallow acceptors, enabling recombination of conduction band electrons with holes trapped at the V_{Zn} states. The calculated energy levels for V_{Zn} are spread in a range from 0.18 to 0.87 eV.[1,14] In our model, we consider V_{Zn} states at $E_V+0.6$ eV to account for the observed position of the DL4 band. Both Zn_i and V_{Zn} levels are positioned relatively shallow in the band gap (see Fig. 3) and thus are likely to follow directly the changes in the electronic structure of the alloy matrix, also explaining the observed blue-

shifts of the DL4 and DL5 bands with increasing Mg content (see Fig. 1 and 2).

On the other hand, the fixed position of the red DL1 band can be understood assuming that the radiative transitions involve electrons trapped at a V_O donor level at $E_V + 2$ eV with valence band holes (see Fig. 3). This assumption is consistent with the reported position of the V_O level at $\sim E_C - 1.3$ eV below the conduction band.[15] Boonchun *et al.*[16] has calculated the band gap position of the V_O states in ZnMgO for Mg concentrations up to 20% and concluded that Mg incorporation might have very little effect on the V_O level. This prediction of a virtually pinned V_O position is in good agreement with our observation of the fixed DL1 band position regardless of the Mg content [see Fig. 2(d)].

Finally, we suggest the DL2 and DL3 bands to be signatures of intrinsic donor-acceptor pair interactions involving shallow donors and O_i and V_{Zn} acceptors, respectively. Indeed, the introduction of an O_i level at $E_V + 0.8$ eV (Refs. 14 and 9) would lead to the observed DL2 band, while a transition via V_{Zn} states would account for the DL3 band. Assuming that the electrons involved in these transitions are supplied by the Zn_i donor level as well as other shallow background donors bound to E_C, we conclude that the redshift in the 2.3 and 2.5 eV bands must be due to a steep rise of the V_{Zn} and O_i positions. However, as discussed above, this is unlikely to be caused by Mg doping in the first approximation. Instead, the redshift in DL2 and DL3 may be readily understood by the introduction of a slightly deeper Mg_i state in the band gap and considering that more Mg_i are created as the doping increases. Assuming that Mg_i related states act similarly to Zn_i as donors, albeit positioned deeper in the band gap, the corresponding donor-acceptor transitions to the O_i and V_{Zn} acceptors would lead to an apparent redshift of the corresponding DL2 and DL3 bands at higher Mg concentrations (shown schematically by coloring variations in corresponding levels in Fig. 3).

In summary, we have studied DLE in ZnMgO films with Mg contents ranging from 0% to 8.5%. Several DL emission components have been resolved at 2, 2.3, 2.5, 2.8, and 3 eV and their shifts have been correlated with Mg incorporation. The red band at 2 eV, associated with oxygen vacancies V_O, does not follow the blueshift trend with increasing Mg content but approximately holds its position. The emission energy of the blue bands at 3 and 2.8 eV does follow the band gap broadening and is assigned to free-to-bound type transitions between Zn_i/V_{Zn} with E_V/E_C edges, respectively. Interestingly, the green bands at 2.3 and 2.5 eV, associated with Zn_i to V_{Zn} and Zn_i to O_i transitions, were found to redshift for higher Mg concentrations. The redshift is interpreted in terms of a competing supply of electrons from slightly deeper Mg_i donor states.

[1]A. Janotti and C. G. Van de Walle, Rep. Prog. Phys. **72**, 126501 (2009).

[2]X. H. Pan, Z. Z. Ye, Y. J. Zeng, X. Q. Gu, J. S. Li, L. P. Zhu, B. H. Zhao, Y. Che, and X. Q. Pan, J. Phys. D: Appl. Phys. **40**, 4241 (2007).

[3]Z. P. Wei, B. Yao, Z. Z. Zhang, Y. M. Lu, D. Z. Shen, B. H. Li, X. H. Wang, J. Y. Zhang, D. X. Zhao, X. W. Fan, and Z. K. Tang, Appl. Phys. Lett. **89**, 102104 (2006).

[4]E. R. Segnit and A. E. Holland, J. Am. Ceram. Soc. **48**, 409 (1965).

[5]K. T. Roro, J. K. Dangbegnon, S. Sivaraya, A. W. R. Leitch, and J. R. Botha, J. Appl. Phys. **103**, 053516 (2008).

[6]D. C. Reynolds, D. C. Look, B. Jogai, C. W. Litton, T. C. Collins, W. Harsch, and G. Cantwell, Phys. Rev. B **57**, 12151 (1998).

[7]H. Li, Y. Z. Zhang, X. J. Pan, T. Wang, and E. Q. Xie, J. Alloys Compd. **472**, 208 (2009).

[8]S. Fujihara, Y. Ogawa, and A. Kasai, Chem. Mater. **16**, 2965 (2004).

[9]X. L. Wu, G. G. Siu, C. L. Fu, and H. C. Ong, Appl. Phys. Lett. **78**, 2285 (2001).

[10]S. A. M. Lima, F. A. Sigoli, M. Jafelicci, and M. R. Davolos, Int. J. Inorg. Mater. **3**, 749 (2001).

[11]E. G. Bylander, J. Appl. Phys. **49**, 1188 (1978).

[12]P. K. Samanta, S. K. Patra, and P. R. Chaudhuri, Physica E (Amsterdam) **41**, 664 (2009).

[13]C. H. Ahn, Y. Y. Kim, D. C. Kim, S. K. Mohanta, and H. K. Cho, J. Appl. Phys. **105**, 013502 (2009).

[14]J. Hu and B. C. Pan, J. Chem. Phys. **129**, 154706 (2008).

[15]Y. M. Sun, P. S. Xu, C. S. Shi, F. Q. Xu, H. B. Pan, and E. D. Lu, J. Electron Spectrosc. Relat. Phenom. **114–116**, 1123 (2001).

[16]A. Boonchun and W. R. L. Lambrecht, Phys. Rev. B **81**, 024103 (2010).

Paper II

Time-resolved spectroscopy of carrier dynamics in graded ZnCdxO multilayer structures

M. Trunk, V. Venkatachalapathy, T. Zhang, A. Azarov, A. Galeckas, and A. Yu. Kuznetsov

Paper III

Carrier dynamics in linearly and step graded Zn$_{1-x}$Cd$_x$O structures

M. Trunk, A. Galeckas, V. Venkatachalapathy, A. Azarov, and A. Yu. Kuznetsov

Carrier dynamics in linearly and step graded bandgap $Zn_{1-x}Cd_xO$ structures

M. Trunk, A. Galeckas[a)], V. Venkatachalapathy, A. Yu. Azarov and A. Yu. Kuznetsov

Department of Physics / Centre for Materials Science and Nanotechnology, University of Oslo,
P.O. Box 1048 Blindern, N-0316, Oslo, Norway

We report on the time-resolved photoluminescence studies of step-like and linearly graded bandgap $ZnCd_xO$ (x=0-60%) structures. The key carrier transport properties essential to the concept of variable bandgap absorbers are addressed, including radiative and nonradiative lifetime, diffusion and drift in the built-in field, and surface and interface recombination. The lifetime parameters are found consistent with the presence of electric field generated by alloying and its gradient with respect to diffusion process. An insight into the depth-resolved lifetime variations is provided, revealing clear correlation with the different degree of lattice mismatch and the resultant deterioration of crystallinity at the interfaces. © *2012 American Institute of Physics.* [DOI: 00.0000/0.0000000]

There is a constant call for more advanced sunlight absorbers in rapidly developing fields of photovoltaics and photo electrochemistry. Among a variety of concepts put forward on how to improve the efficiency of semiconducting photo electrodes [1-3], one possibility relies on the band gap grading, which allows both tweaking of the absorption properties and charge separation of the photo carriers by built-in electric fields. The ternary (Cd, Zn)O alloys appear especially appealing for the role of such advanced absorbers considering the extensive bandgap tunability range covering the ultraviolet and visible parts of the solar spectrum [4]. In spite of a certain maturity of $ZnCd_xO$ bandgap engineering, some critical material properties remain scarcely studied, including carrier transport and lifetime parameters in general and their correlation with alloy composition in particular. Indeed, carrier lifetime is a fundamental physical parameter which determines dynamic properties of semiconductor devices and also ascribes the degree of crystallinity for a given material. The very few studies on the recombination processes in $ZnCd_xO$ reported so far are also sparse in terms of the addressed alloy compositions [5, 6]. The particular importance of a systematic knowledge of the lifetime parameters for variable composition compounds arises from the fact that binary constituents have different crystalline structure (wurtzite for ZnO and rock salt for CdO), and also exhibit low thermodynamic solubility (~2% for CdO in ZnO), both factors pointing towards likely deterioration of crystallinity and phase separation issues for higher Cd-content materials. The role of the interfaces in the carrier transport in a multilayer absorber is yet another key issue calling for clarification. Indeed, bearing in mind the built-in strain due to lattice mismatch of the stacked layers, the interface regions in a step-graded heterostructure appear as potential sites for enhanced carrier recombination, capable of deteriorating the carrier transport properties to a degree unsuitable for practical device applications.

In the present work, we report on the time-resolved photoluminescence (TRPL) studies of carrier dynamics in step-like and linearly graded bandgap $ZnCd_xO$ (x=0-60%) structures. The experiment was devised in a way to allow addressing several key issues of carrier transport individually, including the recombination lifetime parameters (effective, radiative and nonradiative), the roles of carrier diffusion and drift in the built-in field, as well as

surface and interface recombination. To shed more light on the relaxation processes involved, TRPL measurements were carried out in two complementary geometries - by exciting the front-side and the back-side of the graded bandgap layers through the transparent substrate, thus providing all possible combinations of carrier diffusion versus drift directions as well as optically dominant surfaces (front surface versus inner interface). The PL decay transients were monitored at several predefined wavelengths, corresponding to emission from different depth locations of a graded bandgap structure and representing lifetime parameters close to the surface, in the bulk and at the interface region, respectively. A conceptual representation of the energy band diagrams of the investigated structures and two optical geometries used in the PL experiments is shown in Figure 1.

The samples were nominally 250 nm-thick $ZnCd_xO$ structures grown by MOCVD [7] on $c-Al_2O_3$ substrates to represent three different cases of the bandgap alignment: i) a flat bandgap in single layers with fixed (x = 0% and 5%) Cd-content, ii) linearly graded bandgap with high-low (H-L) and low-high (L-H) gradients of Cd content in the films, and iii) step-graded bandgap in the multilayer (ML) structure comprising a stack of 5×50 nm-thick layers with variable Cd-content. A subset of the corresponding samples was annealed at 800ºC for 10 minutes. The actual alloy
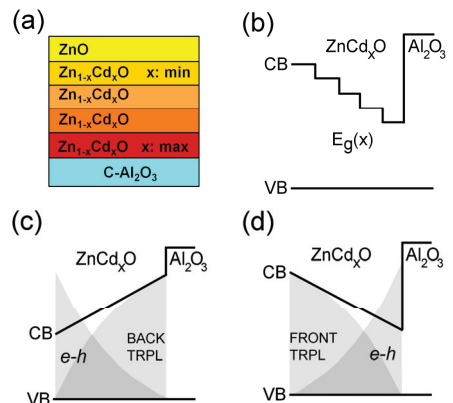

FIG. 1. Schematic representation of the graded bandgap $ZnCd_xO$ structures: (a) growth profile and (b) conceptual band diagram of a step-graded multilayer; (c, d) band arrangements in single layers with high-low and low-high linear variation of Cd content, respectively. The shaded areas signify front- and back-side excitation used in TRPL.

_____

[a)] Author to whom correspondence should be addressed; electronic mail: augustinas.galeckas@fys.uio.no
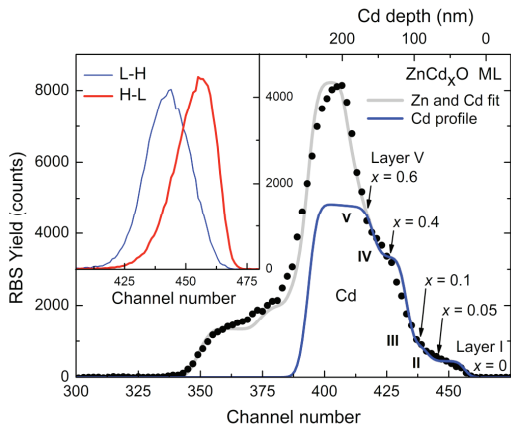
FIG. 2. RBS spectra of a graded bandgap ZnCd$_x$O multilayer structure (5×50nm) revealing the composition and depth distribution of Cd [8]. The inset shows similar data for linearly-graded structures with low-high (L-H) and high-low (H-L) distribution of Cd content with depth, respectively.

FIG. 3. PL spectra obtained at 10K from step- and linearly graded bandgap ZnCd$_x$O structures along with reference spectra of pure ZnO and CdO. The curves are presented in semi-log scale, normalized and shifted vertically for clarity. Hatched vertical bars indicate a set of probe wavelengths used in TRPL experiments. Inset shows the initial carrier profile in step-graded ML under 372nm pulsed laser excitation.

composition in each of the layers was determined by Rutherford back-scattering spectrometry (RBS), yielding Cd concentrations of x = 0, 5, 10, 40 and 60% as illustrated in Fig. 2. Here, the estimated depth scale for Cd distribution is presented on the top of the plot, whereas the inset shows Cd profiles obtained for the linearly graded bandgap structures.

Steady-state PL measurements were performed by employing 325 nm wavelength of cw He-Cd laser (10 mW) as an excitation source. Time-resolved PL was studied by using 372 nm excitation of a picosecond pulsed laser (2mW@40MHz, FWHM 50 ps). The emission was collected by a microscope and directed to a fiber optic spectrometer for steady-state PL (USB4000, Ocean Optics) and to an imaging spectrograph for TRPL (iHR320, Horiba Jobin-Yvon). The transient signals were processed by time-correlated single photon counting technique. Temperature dependent measurements were carried out in the range 10K-300K using a closed-cycle He-refrigerator.

Figure 3 shows time-integrated PL spectra of the step-like and linearly graded bandgap ZnCd$_x$O structures measured at 10K. A characteristic plateau region stretching from 3.2 eV to 2.5 eV in the spectrum of the step-graded ML is comprised of individual near-band-edge emission (NBE) contributions from the different layers in the stack. The excitonic origin of these emission components has been ascertained earlier from the analysis of spectral peak position and intensity dependencies versus excitation intensity and temperature [9]. For linearly graded structures, spectral features in the band-edge region appear less pronounced and merge seamlessly with the broad band of deep-level related emission. The apparent dissimilarities in the time-integrated PL spectra of H-L and L-H structures point towards an intricate relationship between the gradient of alloy composition and optical absorption properties, implying as complex processes of carrier relaxation once probed by a time-resolved PL. Regarding the latter, also noteworthy is the atypical photo-generation profile resulting from the fact that the topmost layer of the step-graded ZnCd$_x$O appears relatively transparent pulsed-laser excitation at 372 nm, whereas the subsequent inner layers exhibit increasingly higher absorption coefficient values. The inset in Fig. 3 shows a numerically simulated initial
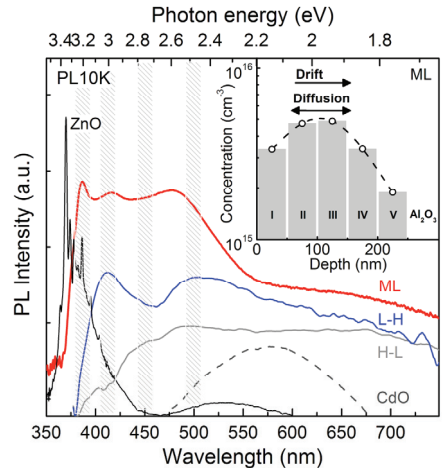
profile of the photo generated carriers in the step-graded ML sample upon 372 nm excitation, indicating that the peak carrier density is shifted from the surface into the depth. The immediate consequence of such off-set is that a few processes have to be considered concurrently in the analysis of the PL transients, including carrier diffusion both towards the surface and into the depth, both ultimately terminated by the non-radiative surface/interface recombination, as well as carrier drift in the built-in field accelerating their escape from the sub-surface region.

The irregular alloy composition and crystallinity make some of the key material parameters hardly predictable, thus rendering impractical the established approach in the analysis of TRPL measurements – numerical modeling and separation of the recombination components from the data fitting. We therefore refer to a comparative analysis of the carrier dynamics with respect to several reference structures with well established properties. Hence, the effect of carrier drift in the built-in field in graded bandgap structures was assessed from the comparison with the flat bandgap case, represented by ZnCd$_x$O single layers with fixed composition (x = 0% and 5% of Cd), whereas the role of multiple interfaces was deduced by contrasting the lifetime parameters of linearly and step-graded structures.

Time-resolved PL measurements were carried out in a broad time scale and at different temperatures. For all investigated ZnCd$_x$O structures, the carrier recombination processes are found to be multi-exponential with characteristic time constants spread in the sub- nanosecond and nanosecond time domains. Figure 4 exemplifies typical PL decay kinetics and corresponding time evolutions of the instantaneous lifetime obtained at 10K from ZnCd$_x$O single layer (x=5%). In the following comparative analysis, only the fastest decay components (τ_1) are considered, yielding typical values in the range of 0.1-0.2 ns for the graded structures against 0.44 ns and 0.34 ns for the flat bandgap ZnCd$_x$O layers with x=0% and 5%, respectively. To put our data into perspective, the longest reported lifetimes of the free exciton emission at 300K spans from 3.8 ns in ZnO
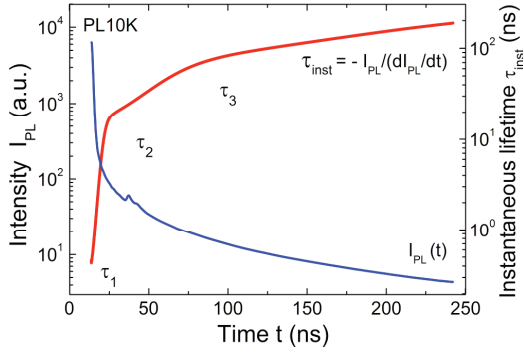
2

FIG. 4. PL decay kinetics of a single ZnCd$_x$O (x=5%) layer and corresponding time evolution of the instantaneous lifetime. The multi-exponential decay can be ascribed by a set of time components (τ_1, τ_2, τ_3).

FIG. 5. Temperature dependencies of PL decay time components (τ_1, τ_2, τ_3) along with the extracted radiative (τ_R) and nonradiative (τ_{NR}) lifetime parameters in a single ZnCd$_x$O (x=5%) layer.

epilayers [9] up to 27 ns in ZnO tetrapods [11], whereas on average ~1ns lifetimes are observed in bulk ZnO [12, 13]. At low temperatures, the bound exciton related PL transients are commonly approximated as biexponential with a fast decay constant reaching up to several hundreds of picoseconds and a slow decay constant in the nanosecond time domain [14]. For ZnCd$_x$O alloys, the PL transients at 2K are reported to be non-exponential with the time constants spanning between 0.2 and 3 ns [5], whereas at room temperature the exciton recombination times reportedly vary from (0.02-0.06) ns [5] to ~1 ns [15].

The measured PL decay time represents the outcome of several competing recombination processes, among which the radiative and non-radiative components have different temperature dependencies, hence can be separated and quantified through a standard procedure described in detail elsewhere [10, 16, 17]. Figure 5 shows temperature dependencies of the PL decay time components along with the extracted radiative and nonradiative lifetime parameters for a single ZnCd$_x$O (x=5%) layer, exemplifying typical to all investigated samples dominance of recombination via nonradiative centers at elevated temperatures. Interestingly, this structure exhibits higher nonradiative lifetime at low temperatures as compared to τ_{NR} ~40 ns estimated for the single ZnCd$_x$O (x=0%) layer or τ_{NR} ~10 ns for the step-graded ML structure.

The depth-resolved features in TRPL measurements of the graded bandgap structures were attained by integrating ~10 nm-wide spectral region around three preselected central wavelengths, namely 410 nm (or 390 nm in the case of ML structure), 450 nm and 500 nm (see Fig. 3). This set
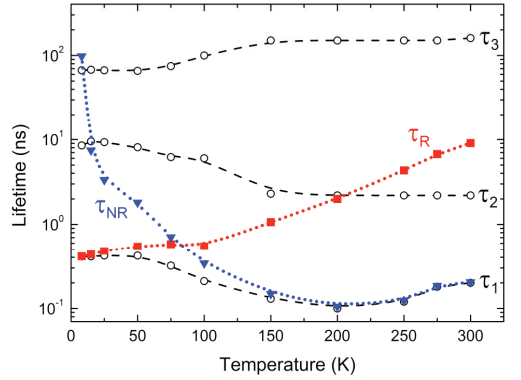
of the probe wavelengths is assumed to represent particular depth locations in the graded structure, which characterize the recombination properties close the surface, in the bulk and near the interface, respectively. In this context, PL decay transients monitored at 500 nm describe the CdO-like side of the linearly graded structure, i.e. with high Cd-content, whereas probing at 410 nm refers to the ZnO-like side (low Cd-content). In both of these cases, TRPL probes the boundary regions, which are expected to be affected either by surface or interface recombination. In contrast, probing at 450 nm traces the recombination processes in the intermediate region, which is least affected by surface effects and thus more closely represents the lifetime parameters attributable to a "bulk" material.

The depth-resolved lifetime parameters measured in as-grown and annealed ZnCd$_x$O structures are summarized in Table I. The revealed variation of the effective lifetimes can be better understood by taking into consideration for each of the presented cases the particular relations of three key factors: i) carrier diffusion – considering different photo-carrier distributions depending on whether CdO-like or ZnO-like side exposed to excitation, ii) carrier drift – considering whether the built-in field is supporting diffusion or directed against the concentration gradient, iii) crystallinity – considering its dependence on the lattice matching degree and alloy composition. Indeed, the numerical simulation of the photo-generation profiles indicates much steeper concentration gradient for the high-Cd content case. Consequently, stronger carrier diffusion

TABLE I. Depth-resolved lifetime parameters τ (ns) in linearly graded, step-graded and flat bandgap ZnCd$_x$O structures as determined by front- and backside TRPL measurements at 10K. The values presented in parenthesis are upon annealing at 800°C for 10 minutes. Arrow symbols indicate mutual orientations of carrier drift and diffusion vectors, **F** and **D**, for each of the cases.

Sample	**F**∥**D**	Surface		Bulk	Interface	
		ZnO-like	CdO-like		ZnO-like	CdO-like
L-H (0-60% Cd)	↑↑	0.23 (0.10)		0.20 (0.40)		0.17 (0.12)
	↑↓	0.40 (0.14)		0.27 (0.41)		0.10 (0.10)
H-L (60-0% Cd)	↑↑		0.11 (0.10)	0.17 (0.33)	0.27 (0.14)	
	↑↓		0.10 (0.06)	0.11 (0.44)	0.17 (0.22)	
ML (0/5/10/40/60% Cd)	↑↑	0.44 (0.25)		0.48 (0.50)		(1.60)
	↑↓	(0.25)		0.90 (0.90)		(1.25)
SL (0% Cd)		0.44 (0.34)		0.44 (0.44)		
SL (5% Cd)		0.42 (0.42)		0.44 (0.44)		

3

into the depth is expected, accordingly diminishing the effective lifetime. Furthermore, because of the carrier localization close to the surface, the role of surface recombination, i.e. non-radiative recombination via surface states, might become considerable in the overall relaxation process. Also, it is reasonable to assume that the high-Cd side potentially represents material of inferior crystallinity due to likely onset of phase separation or alloy content fluctuations. All of these factors indeed have noticeable detrimental effect on the effective lifetime values as follows from the experimental data presented in Table I. Moreover, given that lattice mismatch between c-Al$_2$O$_3$ and ZnO is ~19% and increases further with incorporation of Cd into ZnO, a different degree of crystallinity is expected due to dissimilar residual strain in the interface region of H-L and L-H graded bandgap ZnCd$_x$O layers grown on sapphire substrates [18]. In turn, this implies higher non-radiative recombination loses and correspondingly shorter effective lifetimes in the vicinity of high-Cd content interface compared to that of low-Cd content (ZnO-like), as has indeed been confirmed by the presented experimental results. Similar arguments can be extended to the step-graded bandgap ML containing multiple interfaces, the potentially detrimental role of which can be verified by contrasting depth-resolved lifetime parameters with those of linearly graded structures. As can be seen in Table I, the step-graded ML demonstrates superior time characteristics as compared to other test structures, thus negating any significant implication of the interface recombination in the overall carrier relaxation. This assumption is further supported by the fact of surprisingly high recombination times (~1.6 ns) observed for the carriers confined in the CdO-like region, pointing to a passive role of the boundary with Al$_2$O$_3$ substrate as well. This larger lifetime most likely arise from the localization of the excitons at potential fluctuations produced by alloy disorder. The effect of carrier drift in the built-in field generated by alloying becomes evident from the comparison of the lifetime parameters acquired for two different orientations of the diffusion and electrical field vectors, and also referring to the "flat bandgap" case, represented by ZnCd$_x$O single layers with fixed composition (0% and 5% of Cd). The impact of the bandgap grading on the carrier transport can be estimated referring to so called drift-diffusion length [19]: $L = L_D / ([1 + (q\, F\, L_D /2kT)^2]^{1/2} - q\, F\, L_D /2kT)$, where L_D is carrier diffusion length and F is built-in electric field. Considering common expressions for $L_D = (D\,\tau)^{1/2} = (\tau\,\mu\,kT/q)^{1/2}$ and $F = 1/q\ dE_g/dz$ and assuming a set of approximate input arguments ($\Delta E_g \sim 0.8$ eV bandgap gradient over the d ~250 nm-thickness, carrier lifetime of τ ~1 ns and mobility μ ~1 cm^2 V^{-1} s^{-1}), the above parameters would be of the order of F ~30 kV/cm and $L_D \sim$ 50 nm. This in turn yields the drift-diffusion length of $L \sim$ 300 nm, i.e. carrier transport in the graded bandgap structure is extended by $6 \times L_D$. Another criterion for the built-in electric field to be effective can be expressed as $F > kT/qL_D$, suggesting that the estimated field should be effectual throughout the common for ZnCd$_x$O alloys mobility range of 0.1-1 cm^2 V^{-1} s^{-1} [20].

As a final point, we note that the apparent effects of thermal treatment on the recombination dynamics are for the most part attributable to high mobility and volatility of Cd at elevated temperatures [21], resulting in alloy composition and surface morphology changes, both of these factors having direct impact on the lifetime parameters.

To sum up, an insight into the depth-resolved carrier transport properties in the graded bandgap ZnCd$_x$O structures has been attained by manipulating optical arrangement of the TRPL measurements as well as structure and composition of the purpose-built test samples. The decay time parameters are found consistent with the presence of a strong built-in field and its particular gradient with respect to diffusion process caused by inhomogeneous photo-generated carrier distribution. The observed variation of the recombination times at the interfaces agree well with the different degree of lattice mismatch and the resultant deterioration of crystallinity in this region.

References
[1] T.M. Razykov, C.S. Ferekides, D. Morel, E. Stefanakos, H.S. Ullal, H.M. Upadhyaya, Solar Energy **85**, 1580 (2011).
[2] T. Dittrich, A. Belaidi, A. Ennaoui, Solar Energy Materials and Solar Cells **95**, 6, 1527 (2011).
[3] Yuefan Wei, Lin Ke, Junhua Kong, Hong Liu, Zhihui Jiao, Xuehong Lu, Hejun Du, and Xiao Wei Sun, Nanotechnology **23**, 235401 (2012).
[4] T. Makino, Y. Segawa, M. Kawasaki, A. Ohtomo, R. Shiroki, K. Tamura, T. Yasuda, and H. Koinuma, Appl. Phys. Lett. **78**, 1237 (2001).
[5] I. A. Buyanova, J. P. Bergman, G. Pozina, W. M. Chen, S. Rawal, D. P. Norton, S. J. Pearton, A. Osinsky and J. W. Dong, Appl. Phys. Lett. **90**, 261907 (2007).
[6] B. S. Zou and V. V. Volkov, Chem. Mater. **11**, 3037 (1999).
[7] V. Venkatachalapathy, A. Galeckas, M. Trunk, T. Zhang, A. Azarov, A.Yu. Kuznetsov, Phys. Rev. B **83** 125315 (2011).
[8] RBS spectra were simulated by using SIMNRA code.
[9] M. Trunk, V. Venkatachalapathy, T. Zhang, A. Azarov, A. Galeckas, and A. Yu. Kuznetsov, Phys. Status Solidi C **9**, 1805 (2012).
[10] S. F. Chichibu, T. Onuma, M. Kubota, A. Uedono, T. Sota, A. Tsukazaki, A. Ohtomo, M. Kawasaki, J. Appl. Phys. **99**, 093505 (2006).
[11] Y. Zhong, A. B. Djurisic, Y. F. Hsu, K. S. Wong, G. Brauer, C. C. Ling, and W. K. Chan, J. Phys. Chem. C **112**, 16 286 (2008).
[12] T. Koida, S. F. Chichibu, A. Uedono, A. Tsukazaki, M. Kawasaki, T. Sota, Y. Segawa, and H. Koinuma, Appl. Phys. Lett. **82**, 532 (2003).
[13] A. Teke, Ü. Özgür, S. Doğan, X. Gu, H. Morkoc, B. Nemeth, J. Nause, and H. O. Everitt, Phys. Rev. B **70**, 195207 (2004).
[14] F. Bertram, J. Christen, A. Dadgar, and A. Krost, Appl. Phys. Lett. **90**, 041 917 (2007).
[15] W.F. Yang, Y. N. Xie, Z.Y. Pan, M.H. Hong, Z.Y. Wu, L.M. Wong, S.J. Wang, C.F. Wang, Alex Y.S. Lee and H. Gong, Europhysics Letters (EPL), **99** 27003 (2012).
[16] M. Gurioli, A. Vinattieri, M. Colocci, C. Deparis, J. Massies, G. Neu, A. Bosacchi, and S. Franchi, Phys. Rev. B **44**, 3115 (1991).
[17] M. Kubota, T. Onuma, A. Tsukazaki, A. Ohtomo, M. Kawasaki, T. Sota, and S. F. Chichibu, Appl. Phys. Lett. **90**, 141903 (2007).
[18] J.J. Zhu, T. Aaltonen, V. Venkatachalapathy, A. Galeckas, A. Yu. Kuznetsov, J. Crystal Growth **310**, 5020 (2008).
[19] H.J. Hovel, R.K. Willardson, A.C. Beer (Eds.), Semiconductors and Semimetals, vol. 11 Academic, New York (1975).
[20] C. W. Sun, P. Xin, C. Y. Ma, Z. W. Liu, Q. Y. Zhang, Y. Q. Wang, Z. J. Yin, S. Huang, and T. Chen, Appl. Phys. Lett. **89**, 181923 (2006).
[21] A.Yu. Azarov, T.C. Zhang, B.G. Svensson, and A.Yu. Kuznetsov, Appl. Phys. Lett. **99**, 111903 (2011).

Paper IV

Testing ZnO based photoanodes for PEC applications

M. Trunk, A. Gorzkowska-Sobas, V. Venkatachalapathy, T. Zhang, A. Galeckas, and A. Yu. Kuznetsov